Flow-Induced Crystallization in the Injection Molding of Polymers: A Thermodynamic Approach

Kyuk Hyun Kim, A. I. Isayev, Keehae Kwon

Institute of Polymer Engineering, University of Akron, Akron, Ohio 44325-0301

ABSTRACT: The prediction of the crystallinity and microstructure that develop in injection molding is very important for satisfying the required specifications of molded products. A novel approach to the numerical simulation of the skin-layer thickness and crystallinity in moldings of semicrystalline polymers is proposed. The approach is based on the calculation of the entropy reduction in the oriented melt and the elevated equilibrium melting temperature by means of a nonlinear viscoelastic constitutive equation. The elevation of the equilibrium melting temperature that results from the entropy reduction between the oriented and unoriented melts is used to determine the occurrence of flow-induced crystallization. The crystallization rate enhanced by the flow effect is obtained by the inclusion of the elevated equilibrium melting temperature in the modified Hoffman–Lauritzen equation. Injection-molding experiments at various processing conditions were carried out on polypropylenes of various molecular weights. The thickness of the highly oriented skin layer and the crystallinity in the moldings were measured. The measured data for the microstructures in the moldings agree well with the simulated results. © 2004 Wiley Periodicals, Inc. J Appl Polym Sci 95: 502–523, 2005

Key words: crystallization; injection molding; layer growth; poly(propylene) (PP); rheology

INTRODUCTION

In polymer processing operations such as injection molding, fiber spinning, film blowing, and casting, the molten polymer is subjected to intense shear and elongational flow and crystallizes during the imposition of flow. Because of the flow-induced crystallization, the morphology of the semicrystalline polymer that develops in the final product is typically very different from what is observed as a result of quiescent crystallization of the same polymer. The reduction of entropy between the oriented and unoriented melts, which is due to the molecular chain orientation of the melts, increases the equilibrium melting temperature (T_m^0), and so the crystallization behavior becomes different from that of the unoriented polymer melts. The extent of the T_m^0 increase depends on the degree of orientation in the polymer melt. In other words, the crystallization kinetics are affected by a flow field in the case of an oriented polymer melt.

A number of mathematical models have been proposed for the simulation of quiescent crystallization.[1-8] Most of the nonisothermal crystallization theories[2-4] have been developed from the Avrami–Kolmogoroff theory for isothermal crystallization.[5-8]

Schneider et al.[4] proposed a system of differential first-order rate equations for describing the nonisothermal crystallization kinetics by combining the work of Avrami and Kolmogoroff.[5-8] They developed the kinetics by considering both the formation and growth of nuclei in terms of the system of rate equations. In the limiting case of very fast nucleation with respect to the growth rate, the system of rate equations would reduce to a single rate equation, that is, the Avrami equation for isothermal crystallization.

Nakamura and coworkers[2,3] extended the theories of isothermal crystallization of Avrami and Kolmogoroff[5-8] and Evans[9] on the basis of isokinetic conditions. They suggested a kinetic model of nonisothermal quiescent crystallization, which is customarily cited in the literature as the Nakamura model.

Most of the scientific studies on flow-induced crystallization have been mainly concerned with experimental elucidation and qualitative understanding. Although the basic features of flow-induced crystallization are well known, the quantitative modeling of the process has not been developed significantly. Experimental investigations and theoretical work concerning the development of the morphology and kinetics of flow-induced crystallization have been made by Schultz and coworkers,[10-13] McHugh and coworkers,[14-18] Ziabicki and coworkers,[19-22] and Janeschitz-Kriegl and coworkers.[23-26]

The theoretical work devoted to studying the development of the microstructure associated with flow-

---

Correspondence to: A. I. Isayev (aisayev@uakron.edu)

induced crystallization can be broadly classified into three categories: statistical mechanical models devoted to the equilibrium properties of stretched polymer networks,[27,28] statistical mechanical and classical thermodynamic models devoted to the kinetic properties of the crystallization process,[19] and models connecting the evolution of the morphology with the flow and transport phenomena.[13]

The statistical mechanical model expressing the melting temperature (T_0) elevation was first quantified by Flory[27] in his classic derivation of the equilibrium transition temperature for a stretched, crosslinked system. This model was later modified by Gaylord,[28] who applied the concepts of irreversible thermodynamics to determine the crystallization rates.

Ziabicki[19] and later Janeschitz-Kriegl et al.[25] developed continuum models for flow-induced crystallization based on modifications of the Avrami equation, which contains a phenomenological orientation factor for the effect of flow. Although this approach represents an important advance with respect to the T_0 elevation theory, the resulting models do not couple the rheology of a semicrystalline system with the crystalline kinetics in a predictive way.

Advances in connecting the morphology with the macroscopic properties were made by Schultz,[13] who treated the heat transfer away from a growing crystal front as a rate-determining step.

Shimizu et al.,[29] Katayama and Yoon,[30] and Chen and Spruiell[31] developed mathematical models for flow-induced crystallization to simulate the high-speed fiber-spinning process.

McHugh et al.[14,15,18] developed a model for flow-induced crystallization with the Hamiltonian bracket formulation with the Avrami equation. The model has a number of parameters that can be obtained from rheological measurements and quiescent crystallization experiments.

Yeh and coworkers[32–35] carried out research on flow-induced crystallization from a morphological point of view. They observed a thermally reversible transformation from a fibrillar morphology to a lamellar crystalline morphology in strain-crystallized polymers. They discovered the existence of a nodular structure within perpendicularly oriented lamellae in a glassy, amorphous state.

The flow-induced crystallization behavior is of great industrial importance because solidification phenomena usually take place from a strained melt. A comprehensive study of polyethylene films crystallized from a strained melt has shown a shish-kebab structure similar to that of samples obtained from a stirred dilute solution.[36]

According to the rubber elasticity theory,[37] the molecular origin of elastic force exhibited by a deformed elastomeric network can be expressed by the summation of the internal energy and entropy change contribution. For the formation of temporary entanglements in an elastic liquid, the change in the conformational entropy makes an overwhelming contribution to the variation of the free energy.[37,38]

Haas and Maxwell[39] and Ishizuka and Koyama[40] approached flow-induced crystallization phenomena from a thermodynamic point of view. When polymer chains are under stress influence, entropy reduction takes place. In an oriented melt state, this results in the elevation of T_m^0. By using this elevated melting temperature (T_m), they could determine the flow-enhanced crystallization rate constants.[40]

A great deal of related research has been conducted by Isayev and coworkers.[41–46] They first proposed a method[41,42] for predicting the skin-layer thickness in the injection moldings of isotactic polypropylene (iPP) with the modification of the Janeschitz-Kriegl model of flow-induced crystallization[23–25] and with the Nakamura model of nonisothermal quiescent crystallization.[2,3] They assumed that during the injection-molding process at any material point, there existed a competition between the initiation of flow-induced and quiescent crystallization. In addition, they[47–50] suggested a unified approach to crystallization phenomena under processing conditions. In their model, pure quiescent crystallization is a special case of flow-induced crystallization.

According to their model, the flow-induced crystallization process may take place under or after shearing, being dependent on the effect of supercooling and the intensity of shearing or the evolution of the shearing prehistory during the induction period of crystallization. Flow-induced crystallization can produce a highly oriented shish-kebab crystallite microstructure. However, in the Janeschitz-Kriegl model and its derivative attributable to Isayev et al.,[41,42] flow-induced crystallization is specifically used to refer to cases in which highly oriented lamellar crystallites are produced. In addition, the determination of the model parameters related to flow-induced crystallization requires a tremendous amount of experimental work with a special kind of extrusion experiment.

Recently, Isayev and coworkers[51,52] approached the flow-induced crystallization phenomena from a thermodynamic point of view. They calculated T_m due to the reduction of entropy between the oriented and unoriented melts with the nonlinear viscoelastic constitutive equation.[53] They showed some preliminary results for the prediction of the skin-layer thickness and crystallinity development where the flow-induced crystallization takes place during the filling stage in injection moldings.[51,52]

In this research, a more detailed account is provided on the further development of the model of flow-induced crystallization based on a thermodynamic point of view and a nonlinear viscoelastic constitutive equation along with an increased crystallization rate.

In agreement with Flory,[27] the elevation of T_m^0, which results from the entropy reduction between the unoriented and oriented melts, has been used to determine the occurrence of flow-induced crystallization and the enhancement of the crystallization rate by flow. The crystallization rate enhanced by flow has been included by the incorporation of T_m into the Hoffman–Lauritzen equation.[1] A nonlinear viscoelastic constitutive equation[53] has been used to determine the entropy change and to calculate T_m.

THEORETICAL

Governing equations

The general behavior of the process is described by transport equations: conservation of mass, momentum, and energy. The continuity equation for the flow is

$$\frac{\partial \rho}{\partial t} + \nabla \rho \mathbf{v} = 0 \tag{1}$$

where ρ is the density and $\mathbf{v}$ is the velocity vector.

The momentum equation in a fluid with no body forces is

$$\frac{\partial \rho \mathbf{v}}{\partial t} + \mathbf{v} \times \nabla \rho \mathbf{v} = -\nabla P - \nabla \boldsymbol{\tau} \tag{2}$$

where P is the pressure and $\boldsymbol{\tau}$ is the stress tensor.

A Leonov multimode nonlinear constitutive equation has been used to describe the rheological behavior of polymer melts:[53]

$$\overset{\triangledown}{\mathbf{C}}_k + \frac{1}{2\theta_k}\left[\mathbf{C}_k^2 + \frac{1}{3}(II_C^k - I_C^k)\mathbf{C}_k - \mathbf{I}\right] = 0 \tag{3}$$

where $\mathbf{I}$ is the identity tensor; I_C^k and II_C^k are the first and second invariants of the elastic strain tensor ($\mathbf{C}_k$), respectively; θ_k is the relaxation time; and $\overset{\triangledown}{\mathbf{C}}_k$ is the Jaumann derivative.

In the nonisothermal flow under consideration, the energy equation is

$$\rho C_p\left(\frac{\partial T}{\partial t} + \mathbf{v} \times \nabla T\right) = k\nabla^2 T + \Phi + \dot{Q} \tag{4}$$

where T is the temperature, C_p is the specific heat, k is the thermal conductivity, Φ is the energy dissipation, and $\dot{Q}$ is the rate of heat release due to crystallization per unit of volume. This latter quantity is defined according to the crystallization kinetics as follows:

$$\dot{Q} = \rho X_\infty \Delta H_c \frac{d\theta}{dt} \tag{5}$$

where X_∞ is the ultimate degree of crystallinity, ΔH_c is the heat of fusion for the pure crystal, and θ is the relative degree of crystallinity.

For a viscoelastic flow, Φ is[54]

$$\Phi = 2s\eta_0 tr(\mathbf{E}^2) + \sum_{k=1}^{N}\frac{\eta_k}{4\theta_k^2}\left[\frac{I_C^k(II_C^k - I_C^k)}{3} + tr(\mathbf{C}_k^2) - 3\right] \tag{6}$$

where $\mathbf{E}$ is the deformation-rate tensor, s is the dimensionless rheological parameter lying between zero and unity, η_k is the shear viscosity of the kth mode, and η_0 is the zero-shear-rate viscosity.

$\mathbf{E}$ and η_0 may be expressed as follows:

$$\mathbf{E} = \frac{1}{2}\{\nabla\mathbf{v} + (\nabla\mathbf{v})^T\} \tag{7}$$

$$\eta_0(T) = \frac{\sum_{k=1}^{N}\eta_k(T)}{1 - s} \tag{8}$$

η_k and θ_k are assumed to have an Arrhenius-type temperature dependence:

$$\eta_k(T) = A_k\exp\left(\frac{T_b}{T}\right) \tag{9}$$

$$\theta_k(T) = B_k\exp\left(\frac{T_b}{T}\right) \tag{10}$$

where T_b is the temperature sensitivity of the parameters and is related to the activation energy and A_k and B_k are constants.

These values may increase dramatically as the polymer crystallizes.[55] However, for simplicity, the crystallinity effect on the viscosity and relaxation time has not been considered in this study.

For simple shear, $\mathbf{C}_k$ has the following form:

$$\mathbf{C}_k = \begin{bmatrix} C_{11,k} & C_{12,k} & 0 \\ C_{12,k} & C_{22,k} & 0 \\ 0 & 0 & 1 \end{bmatrix} \tag{11}$$

In this research, the following assumptions have been made for the simulation of the filling stage in an injection-molding process:

1. The thin-film approximation is employed.
2. There is a no-slip condition at the wall.
3. The inertial and body force in the momentum equation are neglected.
4. The pressure is independent of the thickness direction.

5. Thermal conduction in the flow direction is negligible with respect to conduction in the thickness direction.
6. No fountain flow effect at the melt front is considered.

For one-dimensional flow in Cartesian coordinates in the filling stage, the conservation of mass and momentum may be expressed as follows:[56]

$$\frac{\partial}{\partial x}\left(S\frac{\partial P}{\partial x}\right) = 0 \tag{12}$$

where x is the flow direction and S, the fluidity, is defined as

$$S = \int_0^b \frac{y^2}{\eta}\,dy \text{ in Cartesian coordinates} \tag{13}$$

$$S = \frac{1}{2}\int_0^b \frac{r^3}{\eta}\,dr \text{ in cylindrical coordinates}$$

The boundary and initial conditions for the temperature and flow velocity are given by

$$T(y, t < 0) = T_0,\ T(b, t > 0) = T_w,$$

$$\frac{\partial T}{\partial y}(0, t) = 0,\ v_x(b, t) = \frac{\partial v_x}{\partial y}(0, t) = 0 \tag{14}$$

where b is the half-gap of the cavity, T_w is the wall temperature, and v_x is the velocity in the flow direction.

The average velocity (U) can be expressed as follows:

$$U = \frac{1}{b}\int_0^b v_x\,dy \tag{15}$$

According to the N-mode Leonov model, τ is then given by

$$\tau(y, t) = 2\mu\theta_1(T)s\dot{\gamma}\begin{bmatrix} 0 & 1 & 0 \\ 1 & 0 & 0 \\ 0 & 0 & 0 \end{bmatrix}$$

$$+ 2\sum_{k=1}^N \mu_k(T)\begin{bmatrix} C_{11,k} & C_{12,k} & 0 \\ C_{12,k} & C_{22,k} & 0 \\ 0 & 0 & 1 \end{bmatrix} \tag{16}$$

where $\dot{\gamma} = -(\partial v_x/\partial y)$ is the shear rate and $\mu_k = \eta_k/(2\theta_k)$ is the modulus of the kth mode $[\mu = \eta^0/(2\theta_1)]$.

The governing equations for $\mathbf{C}_k$ in eq. (3) can be expressed as follows:

$$\frac{DC_{11,k}}{Dt} - 2C_{12,k}\frac{\partial v_x}{\partial y} + \frac{1}{2\theta_k}(C_{11,k}^2 + C_{12,k}^2 - 1) = 0 \tag{17}$$

$$\frac{DC_{12,k}}{Dt} - C_{22,k}\frac{\partial v_x}{\partial y} + \frac{1}{2\theta_k}(C_{11,k} + C_{22,k})C_{12,k} = 0 \tag{18}$$

$$C_{11,k}C_{22,k} - C_{12,k}^2 = 1 \tag{19}$$

where D/Dt is the material derivative operator.

With the addition of a pressure gradient (Λ_x), the shear stress (τ_{12}) can be expressed as follows:

$$\tau_{12} = \Lambda_x y = \eta\dot{\gamma},\ \Lambda_x = -\frac{\partial P}{\partial x} \tag{20}$$

On the other hand, by integrating eq. (15) by part and eliminating $\dot{\gamma}$ with eq. (20), we find that

$$U = \frac{\Lambda_x}{b}\int_0^b \frac{y^2}{\eta}\,dy = \frac{\Lambda_x}{b}S \tag{21}$$

Accordingly, from eqs. (15), (16), and (20), Λ_x can be expressed as follows:

$$\Lambda_x(t) = \frac{\left(2\mu sbU - 2\sum_{k=1}^N \mu_k \int_0^b \frac{yC_{12,k}}{\theta_1}\,dy\right)}{\int_0^b \frac{y^2}{\theta_1}\,dy} \tag{22}$$

The elastic strain tensor components at a steady-state flow ($\mathbf{C}_k^{st}$) can be expressed as follows:

$$C_{11,k}^{st} = \frac{\sqrt{2}X_k}{\sqrt{1 + X_k}} \tag{23}$$

$$C_{12,k}^{st} = \frac{2\dot{\gamma}X_k}{1 + X_k} \tag{24}$$

$$C_{22,k}^{st} = \frac{\sqrt{2}}{\sqrt{1 + X_k}} \tag{25}$$

where X_k is equal to $1 + \sqrt{1 + 3(\dot{\gamma}\theta_k)^2}$.

The shear viscosity (η) can be expressed as follows:

$$\eta = \eta_0 s + \sum_{k=1}^N \frac{2\eta_k}{1 + \sqrt{1 + 4(\dot{\gamma}\theta_k)^2}} \tag{26}$$

For the calculation of $\mathbf{C}_k$ during the cooling stage, the governing equations for $\mathbf{C}_k$ in eqs. (17)–(19) have been solved by the shear rate being set to zero.

Onset of flow-induced crystallization

For simplicity, instantaneous nucleation is assumed, and this makes the use of a detailed nucleation model unnecessary. Such an assumption has been proposed for flow-induced crystallization in which the crystallization driving forces are large.[57,58]

To determine the highly oriented skin layer developed during the molding process, we must know the onset of flow-induced crystallization. For an oriented polymer melt, the reduction in entropy, due to the orientation of polymer molecules under flow, causes the elevation of T_m^0. According to Flory,[27] T_m can be calculated as follows:

$$\frac{1}{T_m} = \frac{1}{T_m^0} - \frac{\Delta S_{el}}{\Delta H_f} \tag{27}$$

where ΔS_{el} is the change in the entropy and ΔH_f is the change in the enthalpy of crystallization. The value of ΔH_f is the difference between the heat released by crystallization (ΔH_f^m) and the created interfacial energy (ΔH_f^A):

$$\Delta H_f = \Delta H_f^m - \Delta H_f^A = f_{cr}\Delta H_f^m \tag{28}$$

The crystallization factor (f_{cr}) is introduced as the crystallization enthalpy change divided by the heat of crystallization. Evidently, f_{cr} is affected by the created interfacial energy. Therefore, this value, which is unknown, is very important in flow-induced crystallization. As a result, the temperature elevation by the oriented polymer melt can be expressed through the combination of the entropy reduction and heat of crystallization:[51,52]

$$\frac{1}{T_m} = \frac{1}{T_m^0} - \frac{\Delta S_{el}}{f_{cr}\Delta H_f^m} \tag{29}$$

The entropy reduction in eq. (29) is related to the first invariant of the kth mode of $\mathbf{C}_k$ (I_C^k):[51,52]

$$\Delta S_{el} = \sum_k \frac{\mu_k}{T\rho}[I_C^k - 3] \tag{30}$$

where I_C^k is equal to $C_{11,k} + C_{22,k} + C_{33,k}$. This invariant can be obtained by the solution of governing equations for $\mathbf{C}_k$ during filling and cooling stages.

The Flory equation [eq. (27)] is based on equilibrium statistical physics. On the other hand, eq. (30), used for the calculation of entropy reduction, is based on the strain invariant derived from the constitutive equation obtained from irreversible thermodynamics. Therefore, in applying eq. (27), we assume that the nonequilibrium process under any flow condition is driven by undercooling determined from T_m^0.

Flow-enhanced crystallization rate constant

A number of publications concerning various effects observed during the crystallization of polymers in oriented or deformed states have been published. A thermodynamic description, first presented by Flory,[27] was extended by Kobayashi and Nagasawa[59] and Gaylord.[28] These theories predict an increase in T_m^0 mainly due to the entropy reduction of the deformed macromolecular system.

Another attempt at the flow-induced crystallization rate has been reported in the literature; it takes into account the effect of external stress on the rate of crystallization.[21,30,60,61] On a qualitative basis, this effect has been confirmed by many experiments.[40,62,63]

For an oriented melt, the flow-induced crystallization takes place as soon as T_m reaches the local temperature. T_m increases the degree of supercooling and, therefore, speeds up the crystallization process. This means that the elevation of T_0 has the same effect as the supercooling does in the crystallization kinetics. This supercooling effect of flow on the crystallization rate can be incorporated into the nonisothermal Nakamura equation[2,3] through the rate constant determined from the modified Hoffman–Lauritzen equation[1] by the replacement of T_m^0 with T_m.

Ishizuka and Koyama[40] estimated the orientation dependence of the nucleation and growth rate through the replacement of the isotropic T_0 in the nonisothermal crystallization equation with T_m due to the orientation.

Dunning[64] expressed the rate of nucleation as a function of the degree of supercooling by replacing the isotropic T_0 in the nonisothermal crystallization equation with T_m due to the extension and compared this function with experimental data.

Guo and Narh[65] and Isayev et al.[52] applied the modified Hoffman–Lauritzen equation and Nakamura equation to simulate the flow-induced crystallization in the injection-molding process as follows.

The modified Nakamura equation is

$$\frac{D\theta}{Dt} = nK_s(T, \dot{\gamma})(1 - \theta)[-\ln(1 - \theta)]^{(n-1)/n} \tag{31}$$

where n is the Avrami exponent. $K_s(T, \dot{\gamma})$ is the modified nonisothermal crystallization rate constant affected by the shear rate:

$$K_s(T, \dot{\gamma}) = (\ln 2)^{1/n}\left(\frac{1}{t_{1/2}}\right)_0 \exp\left(\frac{-U^*/R}{T - T_\infty}\right)$$

$$\times \exp\left(-\frac{K_k}{T(T_m(T, \dot{\gamma}) - T)f}\right) \tag{32}$$

$$\text{with } f = \frac{2T}{T + T_m(T, \dot{\gamma})}, \quad T_\infty = T_g - 30 \tag{33}$$

TABLE I
Material and Model Parameters Related to the Crystallization Kinetics, Constitutive Equation,
and Thermal Properties of iPPs

Material Constants	PP-6523	PP-6723	PP-6823	Reference
Material specification				
MFI (dg/min)	4.1	0.92	0.51	
PI	4.3	3.9	3.9	
M	351,000	557,000	670,000	
Crystallization kinetics				
$(1/t_{1/2})_0 \times 10^{-8}$ (s^{-1})	5.459	3.858	1.528	46
$K_k \times 10^{-5}$ (K^2)	3.99	3.93	3.81	46
n	3	3	3	
ΔH_c (J/g)	110.56	96.10	91.02	46
X_∞	0.5290	0.4598	0.4355	46
f_{cr}	0.11	0.11	0.11	51
T_m (°C)	172	172	172	70
T_g (°C)	−10	−10	−10	70
Constitutive equation				
s	0.00324	0.000974	0.00118	67
T_b (K)	4,794	4,374	4,548	67
A_1 (Pa s)	2.120×10^{-2}	8.640×10^{-2}	6.180×10^{-2}	67
A_2 (Pa s)	1.820×10^{-1}	11.20×10^{-1}	19.80×10^{-1}	67
A_3 (Pa s)	1.480×10^{-1}	1.80	2.18	67
B_1 (s)	2.800×10^{-7}	8.480×10^{-7}	5.640×10^{-7}	67
B_2 (s)	1.180×10^{-5}	2.340×10^{-5}	4.480×10^{-5}	67
B_3 (s)	3.420×10^{-4}	5.840×10^{-4}	7.280×10^{-4}	67
Thermal properties				
k (W/mK)	0.193	0.193	0.193	70
C_p (J/kgK) $\times 10^{-3}$	2.14	2.14	2.14	70
ρ (kg/m^3)	900	900	900	70

where T_m is from eq. (29), f is the correction factor for the reduction in the latent heat of fusion as the temperature is decreased, R is the universal gas constant, U^* is the activation energy for the segmental jump of polymer molecules and may be assigned a universal value of 6284 J/mol, $(1/t_{1/2})_0$ is the pre-exponential factor that includes all terms influencing the crystallization process but is independent of temperature, and K_k is the nucleation exponent. From eq. (32), it is evident that T_m increases the degree of supercooling and, therefore, the crystallization rate.

EXPERIMENTAL

Materials and sample preparation

The materials were various commercial iPPs with different molecular weights (Pro-fax PP-6523, PP-6723 and PP-6823), which were simply homopolymers with a general-purpose stabilization package from Basell (Lansing, MI). The general material characteristics, including the melt-flow index (MFI), polydispersity index (PI), and weight-average molecular weight (M_w), and model parameters related to the crystallization kinetics, the nonlinear viscoelastic constitutive equation, and the thermal properties are given in Table I.

The injection-molding experiments were performed on a Boy 15S reciprocating-screw injection-

molding machine (Boy Machines Inc., Exton, PA) equipped with a test mold. The standard dumbbell geometry of the mold with the melt-delivery system used in the experiments is shown in Figure 1. Three flush-mounted piezoelectric pressure transducers (Kistler 6153B) were installed to trace the pressure buildup and decay during the injection-molding process. One pressure transducer, P1, was located in the runner. The two others, P2 and P3, were located in the mold cavity. A data-acquisition system, which consisted of an analog/digital converter and a personal computer with Labview software, was used to record the pressure traces during the molding cycle. The injection-molding experiments were carried out under various combinations of the molding conditions. These molding conditions allowed us to establish the effects of the injection speed, T_0, the mold temperature, and the cooling time on the skin-layer thickness and the microstructure of the moldings. The pressure trace within the mold was measured, and f_{cr} was adjusted in such a way that the best fit to the pressure trace was obtained. For iPPs, f_{cr} was 0.11.[51]

Crystallinity and skin-layer thickness

For the crystallinity and morphology investigations, the injection-molded bars were cut for thermal and
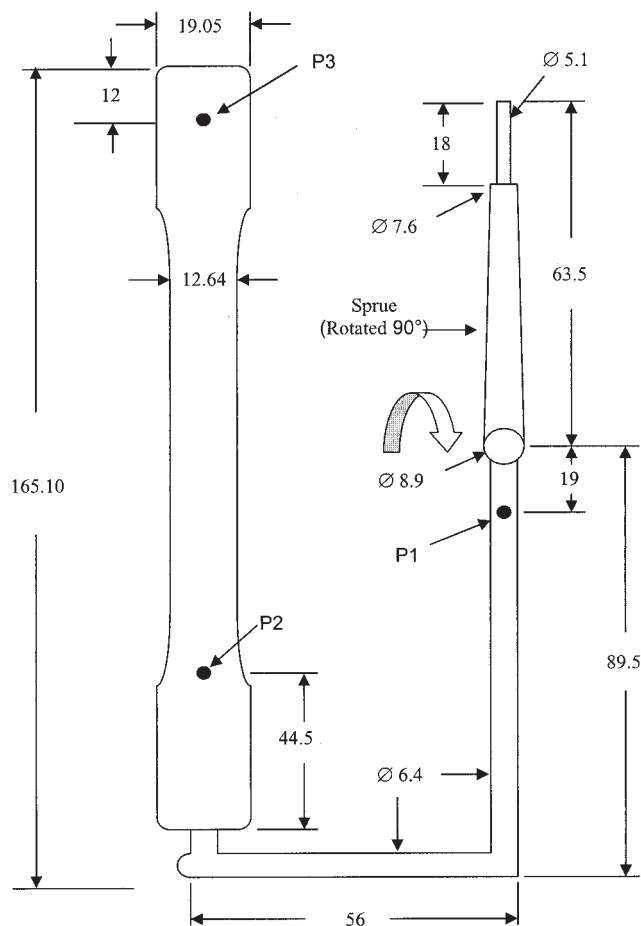
Figure 1 Dimensions of the mold cavity, runner system, and sprue for a dumbbell-shape mold. P1, P2, and P3 are the positions of the pressure transducers. The cross section of the melt-delivery system is circular. The cross section of the gate and cavity is rectangular.

optical analysis, respectively. The thermal analysis was carried out to measure the gapwise crystallinity distribution in the injection moldings with a PerkinElmer DSC-7 (Boston, MA) differential scanning calorimeter. The molded bars were first cut midway in the moldings and then sliced into specimens weighing 1–3 mg at various gapwise locations. The heat flow of the specimens was then obtained as a function of the gapwise location (y) during the DSC thermal analysis. All DSC runs for the specimens were performed at a heating rate of 10°C/min. The gapwise distribution of the absolute degree of crystallinity [$\xi(y)$] at the midpoint of the moldings was calculated on the basis of the heat-flow curve according to the following equation:

$$\xi(y) = \frac{\Delta H_m(y)}{\Delta H_c} \times 100\% \qquad (34)$$

where ΔH_m is the area under the melting peak and ΔH_f^m is the latent heat of fusion for 100% perfect crystals. θ was calculated as follows:

$$\theta(y) = \frac{\Delta H_m(y)}{X_\infty \Delta H_c} \times 100\% \qquad (35)$$

where X_∞ is the ultimate degree of crystallinity for the polymer.

The longitudinal distribution of the skin-layer thickness of the moldings was measured with an Leitz Laborlux 12 POL (McHenry, IL) optical microscope. The specimens used in these measurements were prepared by the cutting of the injection-molded bars. First, a molded bar was cut into five blocks with an electric saw. Each block was cut near the midplane parallel to the x–y plane with a heavy-duty cutter. Then, the sample was cut parallel to the midplane with a diamond saw, and this was followed by cutting with a microtome. The obtained slice of the sample was approximately 20 μm thick. The slice was mounted on a microscope slide. With the optical microscope, the thickness of the highly oriented skin layer was measured as a function of the longitudinal location of x. This thickness was normalized on the basis of the half-thickness of the molded sample.

Quiescent crystallization

To characterize the crystallization kinetics for the various materials used in this study, we used sufficiently dried pellets. Approximately 10 mg of each material was prepared from a pellet and used for both isothermal and nonisothermal crystallization characterization. The isothermal characterization was carried out with the sample in a nitrogen atmosphere with a PerkinElmer DSC-7 differential scanning calorimeter. The sample was first heated from room temperature to a specific temperature (200°C) sufficiently above T_0 and was annealed for 10 min in the DSC furnace to erase any thermal and mechanical history. The melt was cooled at a rate of 50°C/min until the specified crystallization temperature was reached. The half-time ($t_{1/2}$) when half of the final crystallinity was achieved was measured. For the nonisothermal crystallization characterization, the sample was first heated from room temperature to 210°C and was annealed for 10 min in the DSC furnace as in the isothermal case. The melt was then cooled at various rates (2.5, 5, 10, 20, or 40°C/min) down to room temperature, and θ as a function of time and temperature was obtained with a nonisothermal thermogram. Then, by the application of the master-curve approach to crystallization kinetics developed in ref. 66, the experimental rate constants as a function of temperature were obtained. These rate constants were fitted to the Hoffman–Lauritzen equation to determine the crystallization kinetic model parameters [$(1/t_{1/2})_0$ and K_k].

Experimental data and fitted curves for PP-6523, PP-6723, and PP-6823 are presented in Figure 2(a).[46]
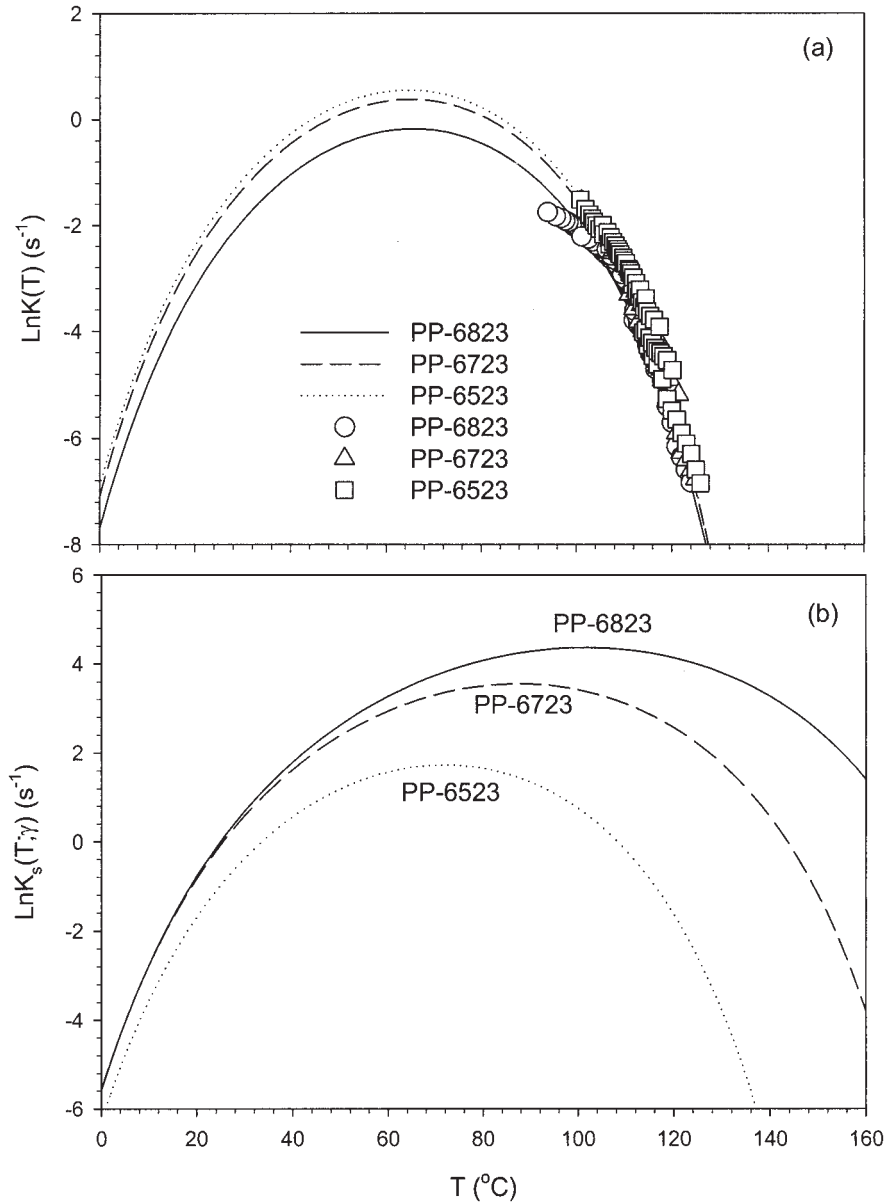
Figure 2 Nonisothermal crystallization rate constants for various iPPs.[46] The experimental data (symbols) with nonlinear regression (lines) are fit (a) to the nonisothermal rate constant under quiescent conditions and (b) to the crystallization rate constants for various iPPs as a function of temperature in the state of flow at $\dot{\gamma} = 500$ s^{-1} and at a processing temperature of 215°C.

Rheological characterization

To calculate the skin-layer thickness and the flow-induced crystallization rate constant on the basis of the thermodynamic crystallization model during the injection molding, we require various material parameters. These include physical, thermal, and rheological properties and the parameter of the crystallization model (Table I). The rheological measurements were performed on a Rheometrics RMS-800 mechanical spectrometer (New Castle, DE) in the cone-and-plate mode within low shear rates ranging from 10^{-2} to 2.0 s^{-1} and on an Instron 3211 capillary rheometer (Canton, MA) within high shear rates from 10 to 10^3 s^{-1}. The material constants, such as s, the number of relaxation mode (N), η_k, and θ_k, were determined from rheological experiments with eqs. (8)–(10) and (26). The material constants, including A_k, B_k, T_b, and s, were obtained by the curve fitting of the viscosity data as a function of the shear rates at three temperatures (180, 200, and 230°C) with the least-square nonlinear regression method. The fitted parameters are listed in Table I. As an example, the measured data along with the fitted curves for PP-6523 are illustrated in Figure 3.[67]
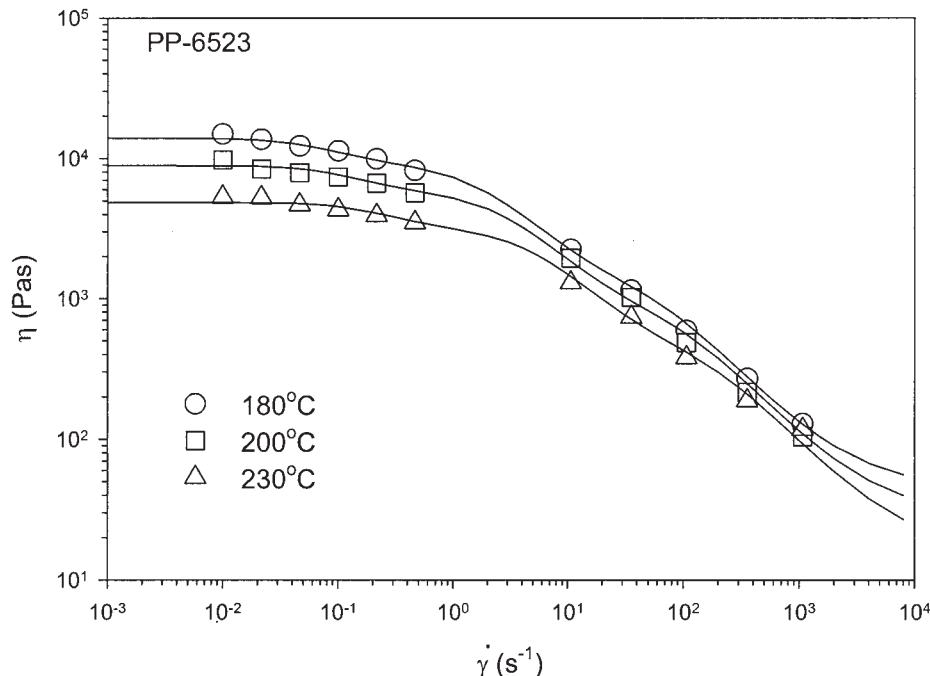
Figure 3 Flow curves at various T_0's as a function of the shear rate for PP-6523. The symbols represent the experimental data,[69] whereas the lines indicate the nonlinear regression fits to eqs. (9), (10), and (26).

The pressure trace within the mold was measured, and f_{cr} was adjusted in such a way that the best fit to the pressure trace was obtained. For iPPs, f_{cr} was 0.11,[51] which showed that the interfacial energy changes caused by the high nucleation density were of the same order as the volume energy changes caused by crystallization. The same f_{cr} value was used to predict the flow-induced crystallized layers of a wide variety of operation points for three iPPs of different molecular weights.

Meshes and numerical scheme

The numerical simulations of the injection-molding process of iPPs were carried out. The simulation code was developed with the ANSI C programming language. The mesh network was generated over the mold cavity and the melt-delivery system, which was divided into 12 segments based on the geometric continuity. None of these segments contained any juncture, with the cross section of the flow channel having the same geometric shape (circular or rectangular). These 12 segments were discretized into 182 equally spaced nodes in the flow direction. The half-thickness in the melt-delivery system and the cavity was discretized into 65 equally spaced nodes.

At the sprue entrance, the gapwise distribution of the temperature is assumed to be uniform and equal to the inlet T_0 value. Presumably, the melt front progresses regularly, starting from the sprue to the end of cavity. That means that the melt front, $x = x_f$,

advances one space of Δx in the time step Δt. The melt front flow can be thought of as the steady, fully developed Poiseuille type. In this case, the system of equations for $\mathbf{C}_k$, composed of eqs. (17)–(19), is reduced from the system of differential equations to that of algebraic equations. The analytical solutions for the $\mathbf{C}_k$ components of the kth mode at the melt front $[C_{ij,k}(x_f, y_j, t)]$, which act as the initial values at the node of (x_f, y_j) for the subsequent time steps, $t + \Delta t$, can be derived as the function of the shear rate in eqs. (23)–(25). At the same time, the shear rates $[\dot{\gamma}(x_f, y_j, t)]$ and the elastic tensor components of the kth mode $[C_{ij,k}(x_f, y_j, t)]$ should satisfy eqs. (16) and (22), as dictated by the viscoelastic constitutive equation and transport laws. Therefore, eqs. (16), (22), and (23)–(25) can be considered the system of equations for the shear rate $[\dot{\gamma}(x_f, y_j, t)]$, which can be solved by the Newton–Raphson iterative method.[68] The initial guess for the shear rate $[\dot{\gamma}(x_f, y_j, t)]$, is given by

$$\dot{\gamma}^0(x_f, y_j, t) = \frac{3U}{b^2} y_j \text{ (Cartesian coordinates)} \quad (36)$$

$$\dot{\gamma}^0(x_f, y_j, t) = \frac{4U}{b^2} y_j \text{ (cylindrical coordinates)} \quad (37)$$

Starting from the initial guess so determined, we applied the iterative solution procedure based on the Newton–Raphson method until the solutions for the elastic strain tensors and shear rates at the melt front converged.
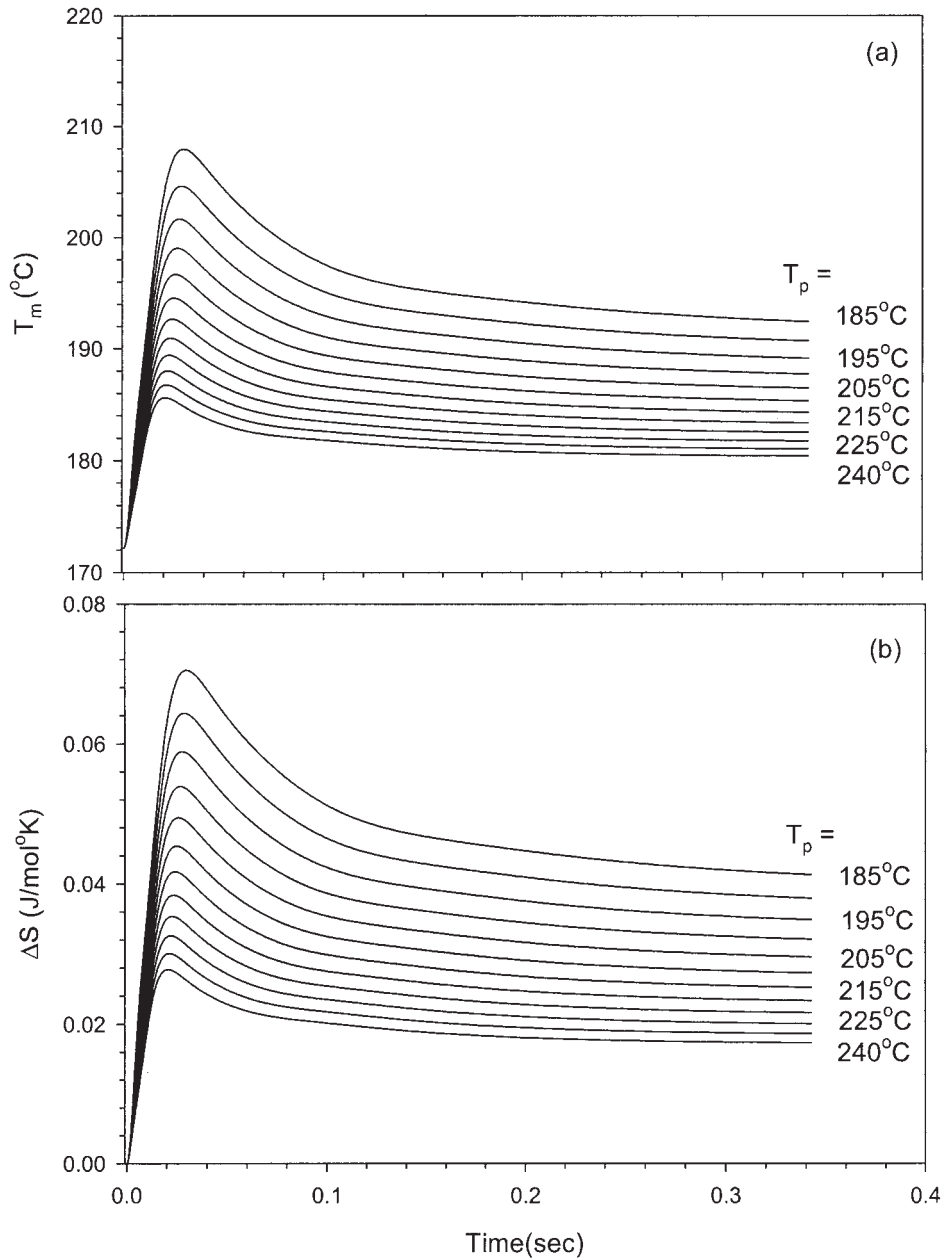
Figure 4 (a) Transient T_m elevation and (b) transient entropy reduction (ΔS) after the startup of isothermal shear flow at $\dot{\gamma}$ = 500 s^{-1} at various processing temperatures (T_p's) for PP-6523.

In computation, the melt front moves along the flow direction until it reaches the end of the cavity. For nodes other than those at the melt front and the gate in the flow domain, (x_i, y_i) with $i \neq f$, which are termed *internal nodes*, the iterative method with the numerical relaxation must be used to directly solve the system of equations composed of eqs. (16), (22), and (17)–(19), with $C_{ij,k}(x_i, y_j, t)$ and $\dot{\gamma}(x_i, y_j, t)$ at the node as the unknowns. The initial guess for each of the unknowns is its value at the previous time, namely, $C_{ij,k}(x_i, y_j, t - \Delta t)$ and $\dot{\gamma}(x_i, y_j, t - \Delta t)$. The shear rates and the elastic strain tensor components are numerically determined with the convergence parameters.

The convective term in eqs. (17) and (18) was handled with newly calculated time step, $\Delta t'$, by the consideration of flow in the filling stage:

$$\Delta t' = \frac{1}{1/\Delta t + u(x_i, y_j, t)/\Delta x} \tag{38}$$

With the converged value of $C_{ij,k}(x_i, y_j, t)$, $\tau(x_i, y_j, t)$, $\Delta S_{el}(x_i, y_j, t)$, $v(x_i, y_j, t)$, and $\theta(x_i, y_j, t)$ can be updated. After the mold cavity is filled completely, the cooling stage starts.

In the cooling stage, the flow field presumably vanishes. The velocity and shear rates are set to zero. The
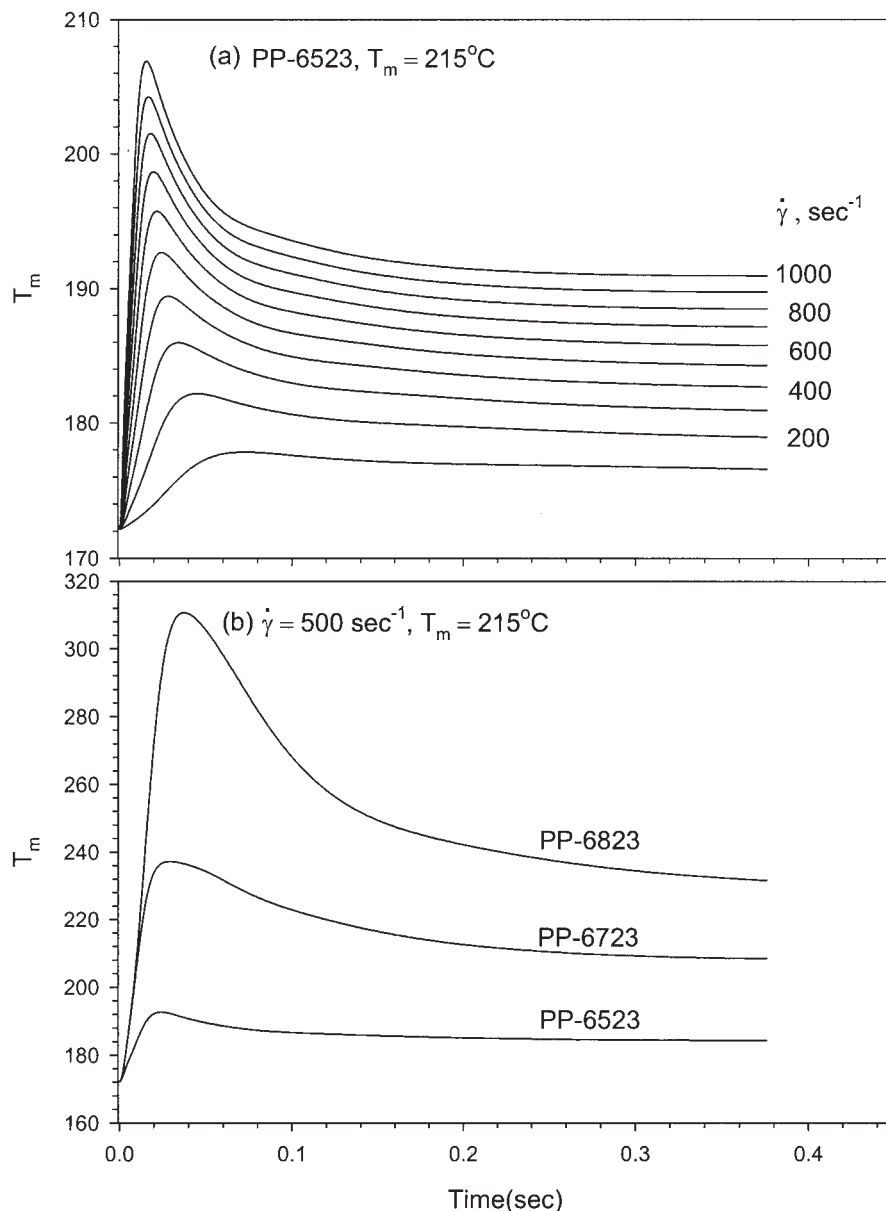
Figure 5 Transient T_m^0 values for (a) PP-6523 at various shear rates and at a processing temperature of 215°C and (b) PPs of various molecular weights at $\dot\gamma = 500$ and at a processing temperature of 215°C as a function of time after the startup of isothermal shear flow.

flow stresses that developed during the filling stage relax, governed by the viscoelastic constitutive equation [eqs. (17)–(19)]. Therefore, the numerical computation scheme for the relaxation of the flow stresses is greatly simplified in comparison with that of the filling stage. The computational procedure is similar to that explained in the filling stage, except that the calculations related to the flow field disappear with $\dot\gamma = \nu_x \equiv 0$.

The skin-layer thickness was determined by a comparison of T_m determined from eq. (29) with the local T_0 value calculated from eq. (4). When T_m is equal to the local temperature, flow-induced crystallization

takes place. For fast-crystallizing polymers such as iPP, the viscosity increases tremendously, and the orientation and elastic strain that result from the stress at that moment freezes, and a highly oriented skin layer forms. Because of the elevation of T_m^0, the degree of supercooling increases, and so the rate of crystallization increases conspicuously. The simulated results under various molding conditions for various iPPs were compared with the measured data in an attempt to understand the mechanism for the development of the skin layer and crystallinity. The influences of the molecular weight and the molding conditions on the final morphology were investigated.
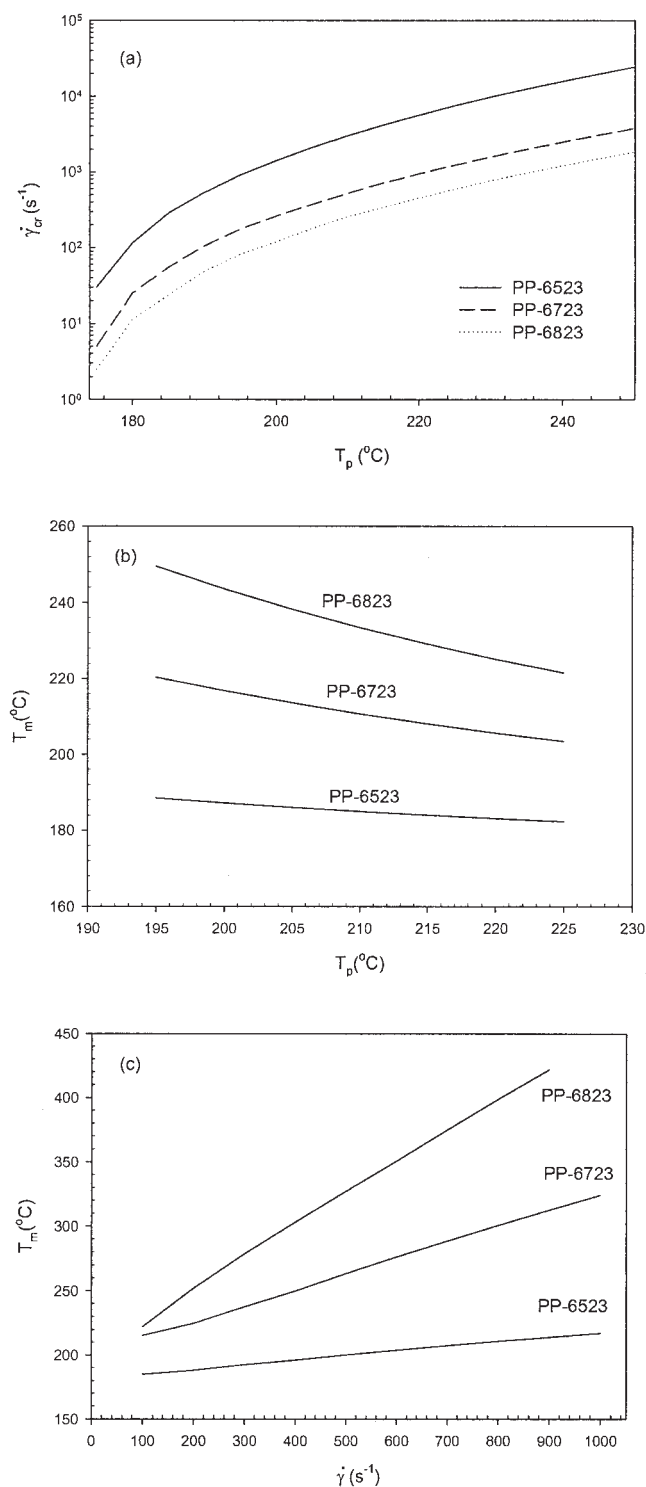
Figure 6 (a) Critical shear rates, (b) T_m as a function of the processing temperature (T_p) at $\dot{\gamma} = 500$, and (c) T_m as a function of the shear rate at $T_p = 215°C$ for PP-6523, PP-6723, and PP-6823.

RESULTS AND DISCUSSION

T_m^0 elevation under isothermal conditions

The entropy change (ΔS_{el}) reflects the energy change associated with the change in the molecular arrange-ments. The higher the orientation is of the polymer melts, the lower the number is of possible arrange-ments available to the segments of the polymer mol-ecules. The degree of orientation affects the entropy between the unoriented and oriented melt in the equi-librium state.

The entropy reduction can be obtained from eq. (30) on the basis of the calculated first invariant of $\mathbf{C}_k$. $\mathbf{C}_k$ is a function of time, temperature, and shear rate. Figure 4 illustrates the transient T_m values according to eqs. (29) and (30) and the transient entropy reduction due to eq. (30) after the startup of isothermal shear flow at the constant shear rate of 500 s^{-1} and at various pro-cessing temperatures for PP-6523. Figure 4(a) shows that the transient T_m^0 value first increases linearly with time at small times, then deviates from the linearity and overshoots, and finally reaches a steady-state value, which is higher at the lower processing temper-ature. The sharp increase in the entropy reduction during the early stage, shown in Figure 4(b), comes from the elasticity of the polymer melt, whereas the steady-state entropy change happens when the relax-ation behavior is completed. The tendencies of en-tropy reduction and T_m^0 elevation are very similar because the T_m elevation is calculated from the en-tropy reduction.

Figure 5(a) shows the transient T_m^0 elevation as a function of time for PP-6523 at various shear rates and a constant processing temperature of 215°C. T_m^0 in-creases with the shear rate because at high shear rates stresses increase and induce high molecular orienta-tion and, therefore, entropy change. The degree of T_0 elevation is predominant for high-molecular-weight PP-6823. This is shown in Figure 5(b), which indicates the transient T_m^0 values of polypropylenes (PPs) of various molecular weights at a constant shear rate of 500 s^{-1} and at a processing temperature of 215°C. Evidently, the entropy reduction level increases with the molecular weight and the magnitude of the shear rate and decreases with an increase in the processing temperature. A higher stress level is needed to achieve the same magnitude of the shear rate for high-molec-ular-weight PP. This high stress level increases the degree of T_m elevation.

Figure 6(a) shows the critical shear rate as a func-tion of the processing temperature for PP-6523, PP-6723, and PP-6823. The critical shear rate is defined here as the shear rate at which flow-induced crys-tallization takes place. The critical shear rate in-creases with the processing temperature because the stress level for the same shear rate is lower at a high processing temperature. In addition, the critical shear rate is higher for PP-6523 than for PP-6823 because of the lower relaxation time and viscosity and, therefore, the extent of entropy change for PP-6523. A higher shear rate is needed for the flow-induced crystallization of PP-6523, which has a
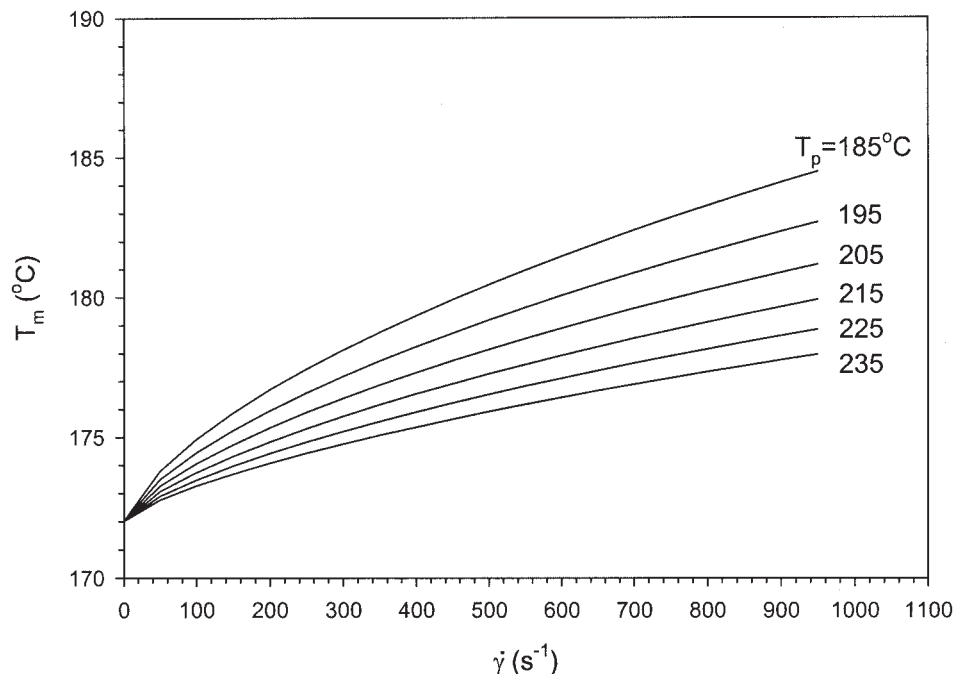
Figure 7 T_m versus the shear rates at various processing temperatures (T_p's) for PP-6523.

lower relaxation time. The effect of the molecular weight on the elevation of T_m^0 versus the processing temperature at a constant shear rate of 500 s^{-1} is illustrated in Figure 6(b). Clearly, the extent of elevation of T_m^0 increases with an increase in the molecular weight. The extent of elevation of T_m^0 of PP-6523 is lesser because of the lower stress level attained in the sample of the low molecular weight, and it becomes smaller at a higher processing temperature for the same reason.

Figure 6(c) demonstrates the elevation of T_m^0 as a function of the shear rates for PP-6523, PP-6723, and PP-6823 at a constant processing temperature of 215°C. At the same shear rate, the elevation of T_m^0 is higher for higher molecular weight PP and increases with the shear rate. High-molecular-weight PP, such as PP-6823, has a higher relaxation time, and the extent of the elevation of T_m^0 is higher than that of low-molecular-weight PP.

Figure 7 shows the elevation of T_m^0 versus the shear rates at various processing temperatures for PP-6523. T_m decreases as the processing temperature increases. When the processing temperature increases, the relaxation time of the polymer melts decreases. Accordingly, T_m decreases at the same shear rate when the processing temperature increases.

Flow-induced crystallization

For an oriented melt, flow-induced crystallization takes place as soon as T_m reaches the local temperature. T_m increases the degree of supercooling and so

speeds up the crystallization process. This means that the elevation of T_0 has the same effect as supercooling does in crystallization kinetics. This supercooling effect of flow on the crystallization was incorporated into the nonisothermal Nakamura equation [eq. (31)] through the rate constant determined from the modified Hoffman–Lauritzen equation by the replacement of T_m^0 with T_m in eq. (32).

The crystallization phenomena can be explained by two factors, such as the stress and degree of supercooling. Through the substitution of the isotropic T_m^0 value with T_m, the crystallization rate described by the Hoffman–Lauritzen equation can be enhanced by the effect of flow.[39,40,52] As a result, the flow increases the degree of supercooling and the crystallization rate as well and makes the position of the highest crystallization rate shift to the higher temperature.

Figure 2(a) shows the measured and calculated crystallization rate constants in the quiescent state for iPPs of different molecular weights. In the quiescent state, the crystallization rate of PP-6523 is higher than that of PP-6723 or PP-6823. This is because of the difference in the mobilities of the molecular chains. However, when the flow is imposed upon the polymer melt, the increase in the crystallization rate is predominant fir PP-6823. This is illustrated in Figure 2(b), which shows the calculated rate constant as a function of the crystallization temperature at a shear rate of 500 and at a processing temperature of 215°C for PP-6523, PP-6723, and PP-6823. The flow effect on the crystallization rate is tremendous, especially for PP-6823, because of the
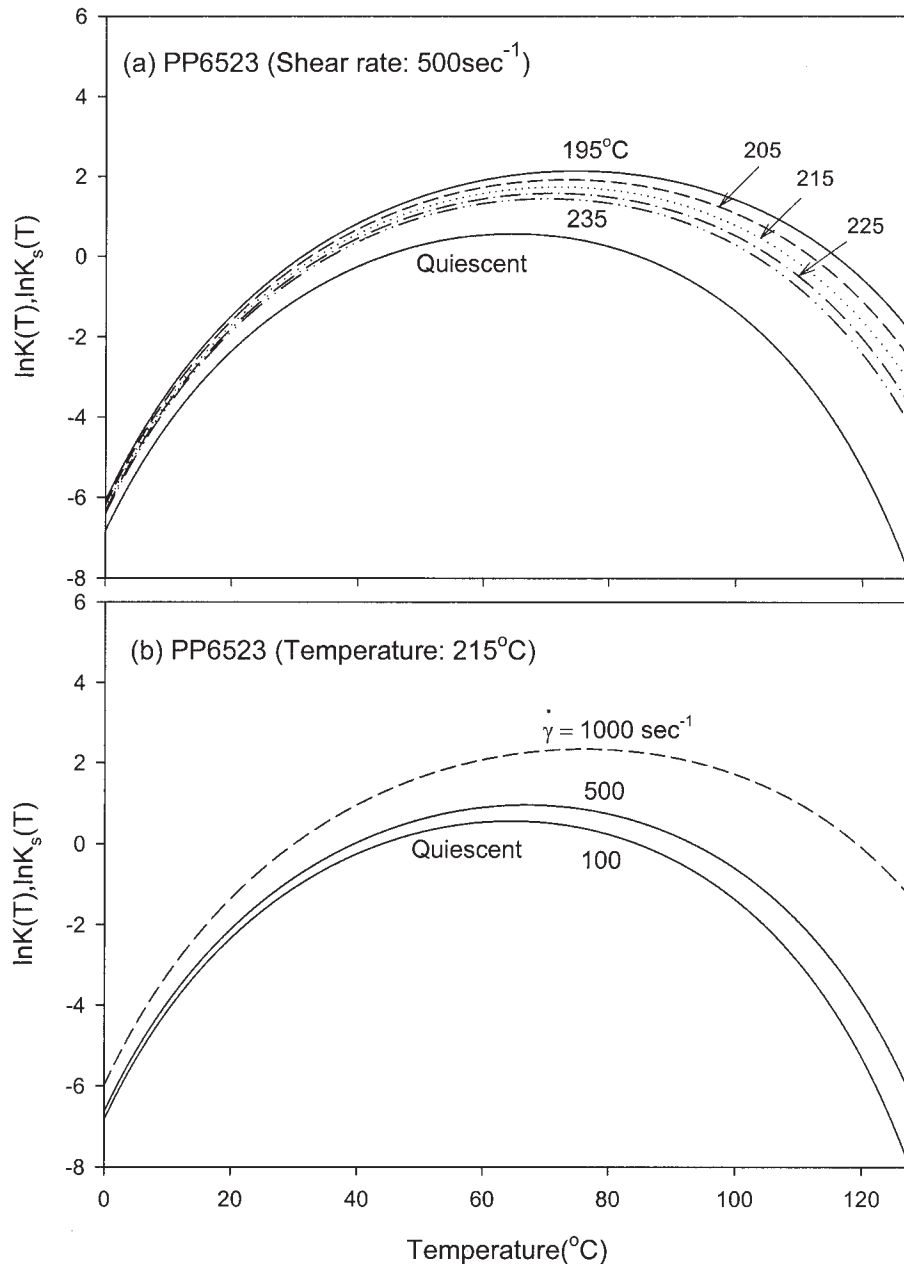
Figure 8 Crystallization rate constant as a function of the crystallization temperature (a) at different processing temperatures at $\dot{\gamma} = 500 \text{ s}^{-1}$ and (b) at different shear rates at a processing temperature of 215°C for PP-6523 for quiescent and flow-induced crystallization.

higher relaxation time and greater enhancement of the rate constant than for low-molecular-weight PP-6523.

Figure 8 shows the calculated crystallization rate constant as a function of the crystallization temperature at different processing temperatures and a constant shear rate of 500 and at different shear rates and a constant processing temperature of 215°C for PP-6523 for both quiescent and flow-induced crystallization. Because of the reduction of entropy during flow, the crystallization rate and its maximum increase with an increasing shear rate and a decreasing processing temperature, with the

position of the maximum shifting to higher temperatures.

Figure 9 demonstrates the calculated maximum crystallization temperature and rate constant as functions of the shear rate at a constant processing temperature of 215°C for PP-6523, PP-6723, and PP-6823. The maxima of the rate constant and crystallization temperature increase with the shear rate. The increase is more predominant for high-molecular-weight samples. Among the various iPPs, the rate constant of PP-6523 is the highest in the quiescent state but becomes the lowest above a certain shear rate.
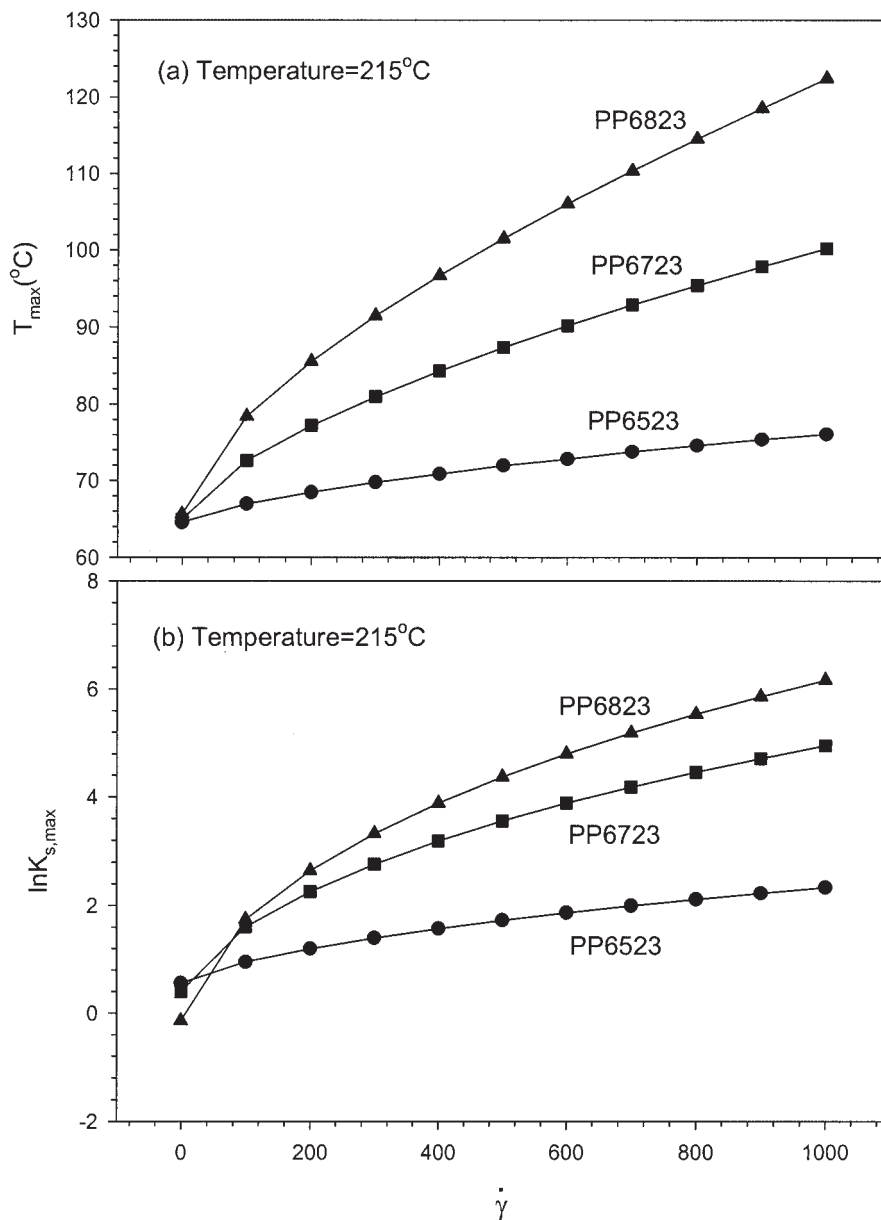
Figure 9   (a) Maximum crystallization temperature (T_{max}) and (b) maximum rate constant ($K_{s,max}$) as functions of the shear rate at a processing temperature of 215°C for PP-6523, PP-6723, and PP-6823.

Figure 10 shows the effect of the shear rate on the degree of supercooling at various processing temperatures for PP-6823 and at a constant processing temperature of 180°C for various iPPs. The effect of the shear rate on the degree of supercooling is conspicuous for high-molecular-weight PP-6823 in Figure 10(b) and at a low processing temperature in Figure 10(a) because of the high relaxation time.

Figure 11 shows the development of θ under quiescent conditions and at various shear rates at a processing temperature of 215°C under isothermal conditions corresponding to the maximum crystallization rate for PP-6523 and at a constant shear rate of 200 s^{-1} and a processing temperature of 215°C for PP-6523, PP-6723, and PP-6823. The flow effect on

the development of crystallinity manifests itself in the acceleration of crystallization, such that at a shear rate of 1000 s^{-1}, the development of crystallinity is complete within 0.2 s [Fig. 11(a)]. At the same shear rate, the development of crystallinity is more predominant for high-molecular-weight PP, as shown in Figure 11(b).

Flow-induced layer and crystallinity in injection molding

During the filling stage, a high shear rate near the wall allows polymer molecules to be aligned along the flow direction. If the shear rate exceeds the critical shear rate, flow-induced crystallization takes place. For fast-
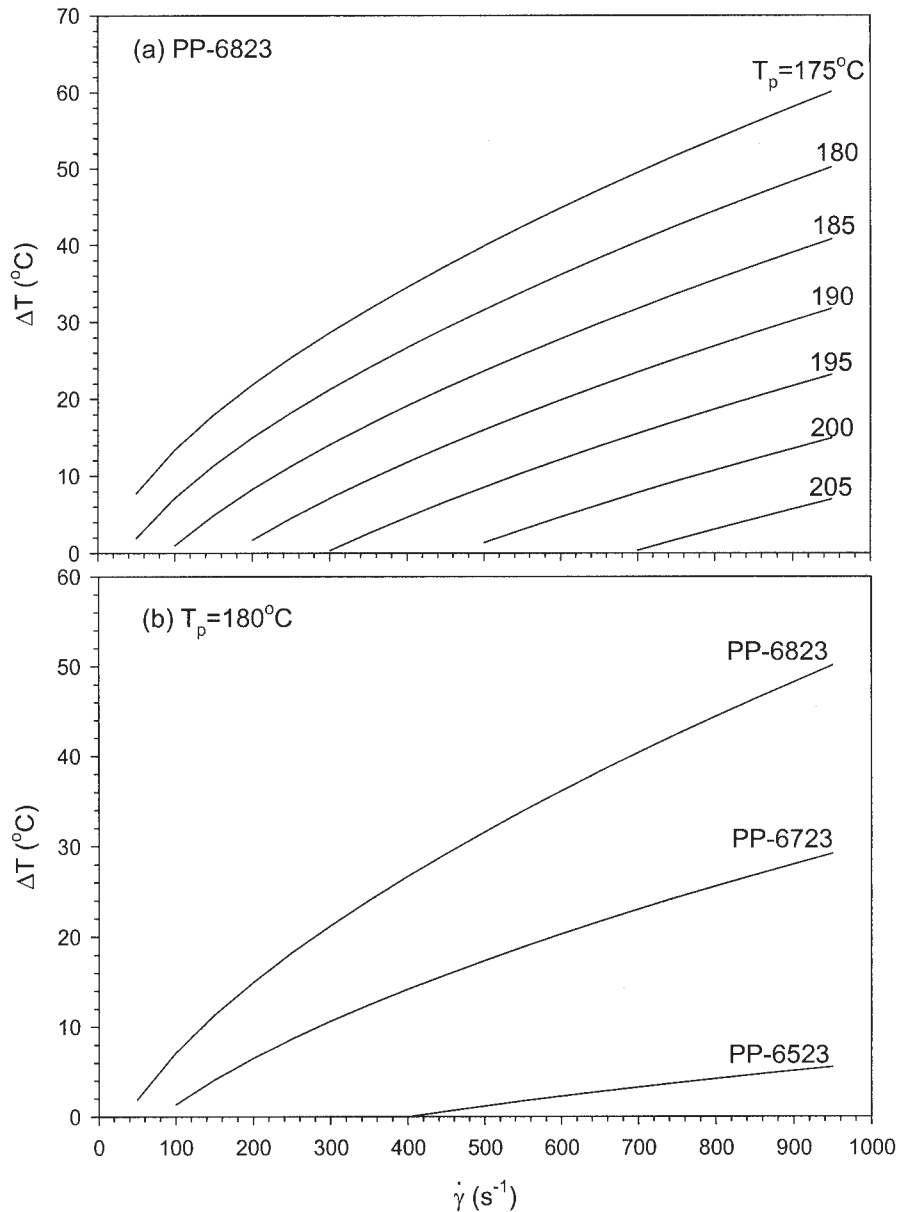
Figure 10 (a) Effect of the shear rate on the degree of supercooling (ΔT) at various processing temperatures for PP-6523 and (b) effect of the shear rate on ΔT for various iPPs at a processing temperature of 215°C.

crystallizing polymers such as iPPs, the experimentally measured final relative crystallinity in the moldings was 100% at every point. The simulated data also show these results.

Figure 12 demonstrates the gapwise distribution of θ of PP-6523 at the middle of the cavity at various times for PP-6523 and for various iPPs at times of 13.125 and 23.025 s. The crystallinity develops very quickly in the skin layer because of the accelerating effect of flow on crystallization. For the case depicted in Figure 12(a), it took less than 13 s for θ to reach 100% at every gapwise location within the skin layer of the molding, whereas at the locations close to the mold wall, it took just about 2 s. This indicates that

shortly after the melt is in its supercooled state, θ at the locations close to the mold wall jumps to 100%. Within the core region, the cooling by the cold mold is less effective because the gapwise locations are farther from the wall. At the same time, the accelerating effect of flow on crystallization becomes less pronounced and eventually vanishes somewhere in the core region. Consequently, the time for the completion of crystallization becomes longer. Figure 12(a) shows that at the locations close to the center of the molding, even after 23 s, the crystallization does not complete.

Figure 12(b) shows that PP-6523 develops most quickly with respect to crystallinity, whereas PP-6823 shows the slowest development in crystallinity. Times
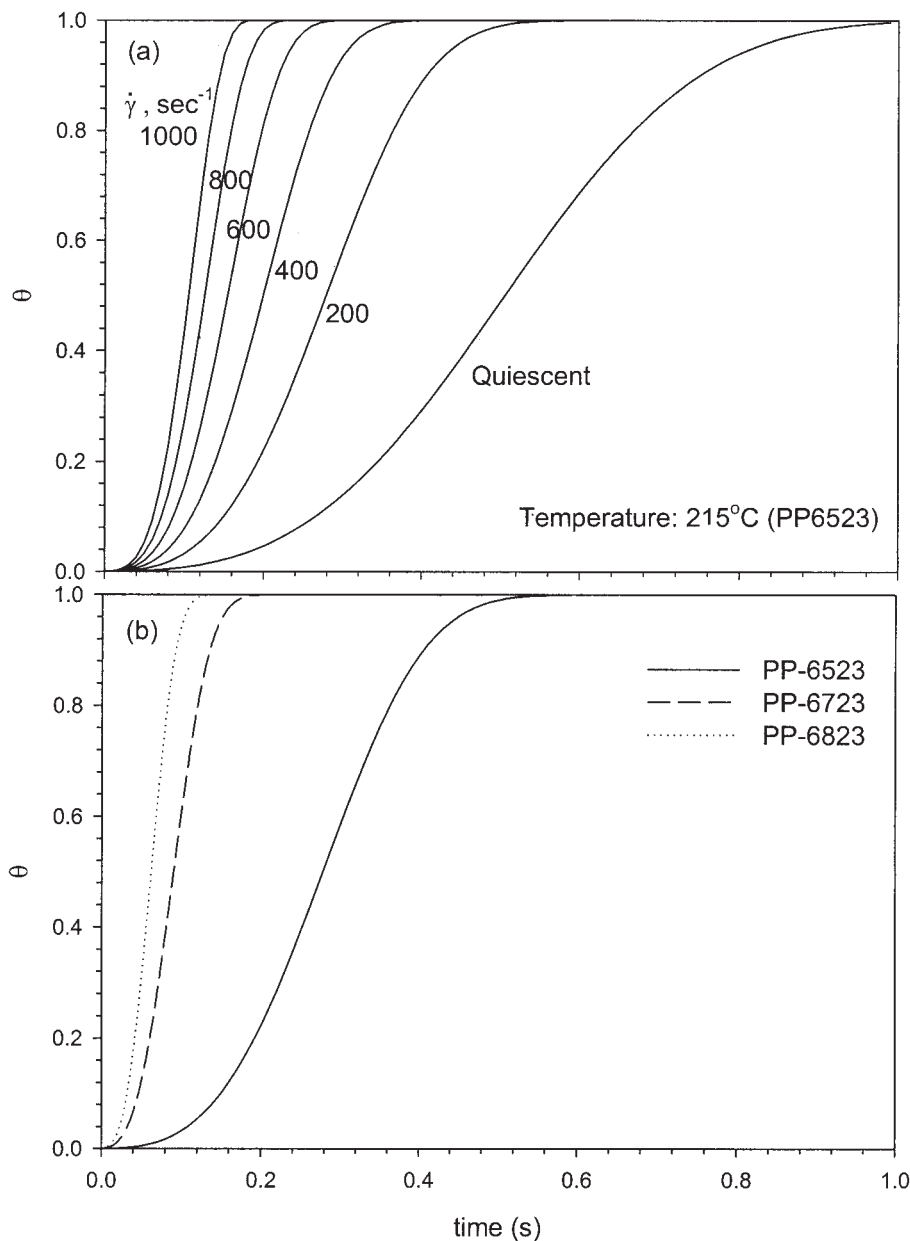
Figure 11 θ development under the quiescent conditions and various shear rates under the isothermal conditions of a maximum crystallization rate constant (a) for PP-6523 at a processing temperature of 215°C and (b) for PP-6523, PP-6723, and PP-6823 at $\dot{\gamma} = 200$ s^{-1} and at a processing temperature of 215°C.

of 13.125 and 23.025 s correspond to the packing stage. In this stage, PP-6523 experiences a higher shear rate because of its lower melt viscosity. Thus, it provides faster crystallinity development. From the simulated results of the development of crystallinity during the molding cycle, an idea concerning the optimum molding time may be obtained with the aim of optimizing the processing conditions.

Figure 13 shows the skin-layer development during the filling stage for PP-6523 and PP-6823. During cavity filling, the maximum of the skin-layer thickness increases with the filling time until the cavity is filled. The position of the maximum skin layer moves farther

away from the cavity entrance. A comparison of Figure 13(a) and Figure 13(b) indicates that the skin-layer development is more predominant for PP-6823. This is due to the higher relaxation time and viscosity and entropy reduction for the high-molecular-weight sample contributing to the higher elevation of T_m^0 and greater enhancement of flow-induced crystallization and, therefore, the thicker layer.

Figure 14 presents the measured[67] and predicted skin-layer thicknesses as a function of the distance from the gate (x) for PP-6523 moldings obtained at various inlet T_0 values, mold-wall temperatures, and injection speeds. The agreement between the
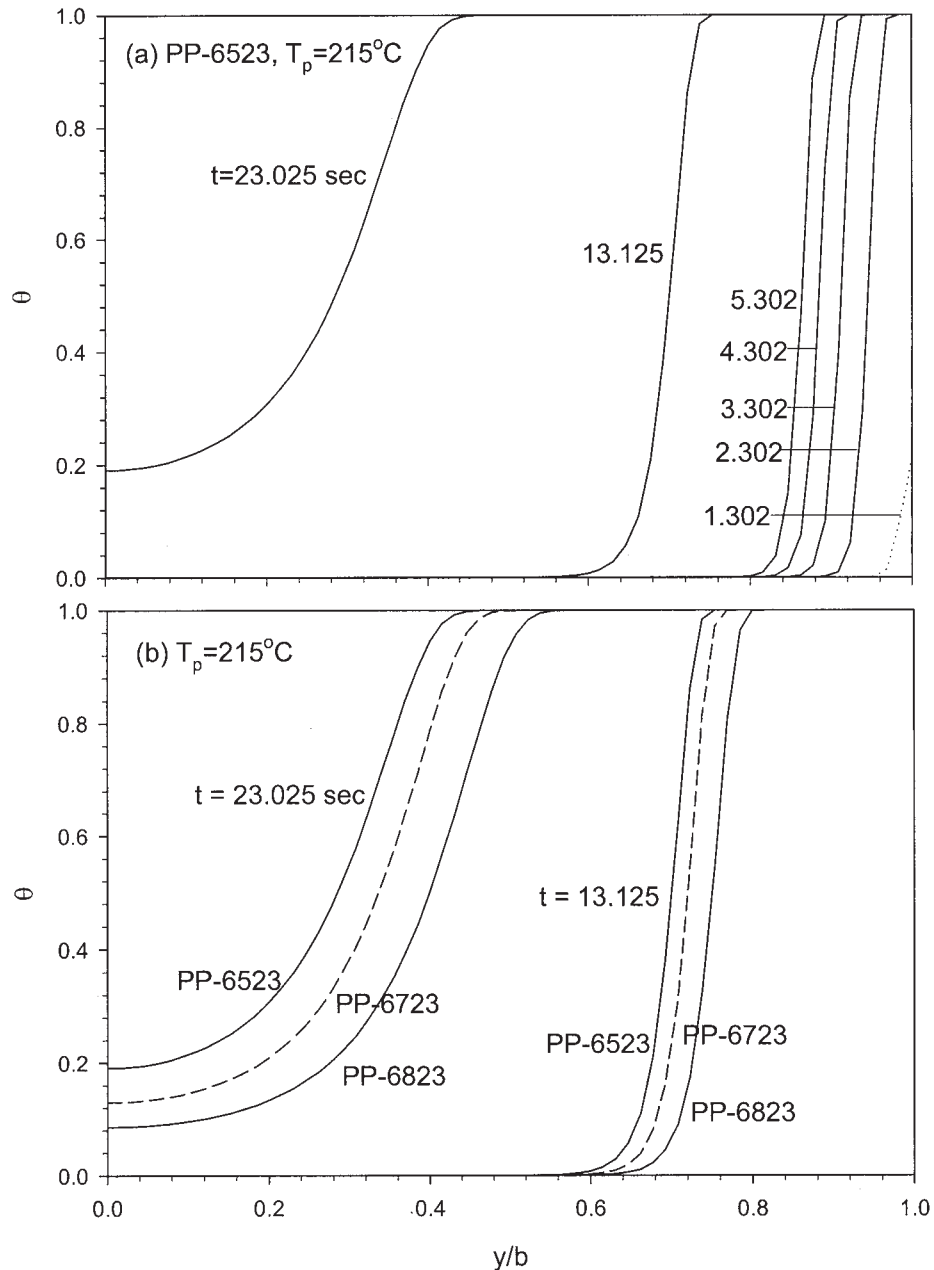
Figure 12 Gapwise distribution of θ at the midway of a dumbbell-shaped cavity and various times for (a) PP-6523 and (b) for various iPPs at times of 13.125 and 23.025 s. The molding conditions were $Q = 12.7 \text{ cm}^3/\text{s}$, $T_w = 60°C$, $t_h = 45$ s, and $T_0 = 215°C$.

measured and predicted results is quite good. Generally, the skin-layer thickness increases with x, goes through the maximum at the intermediate location in the cavity, and then decreases toward its end.

The effect of the inlet T_0 value on the skin-layer thickness is illustrated in Figure 14(a). As the inlet T_0 values increases, the local temperature of every point in the cavity is higher, and this results in a higher critical shear rate required to achieve a T_0 elevation equal to the local temperature. Therefore, it is more difficult for flow-induced crystallization to take place.

Also, a thinner skin-layer thickness is expected. In addition, because of the low relaxation time at a high local temperature, it is more difficult for flow-induced crystallization to occur. Therefore, through the adjustment of the inlet T_0 value, the skin-layer thickness can be controlled. If the temperature is not too high for thermal degradation to occur, T_0 can be a good parameter for reducing anisotropic properties because of the presence of a skin–core structure in the moldings.

Figure 14(b) shows the effect of the mold temperature on the development of the skin layer. Both the experimental and simulated results demonstrate an
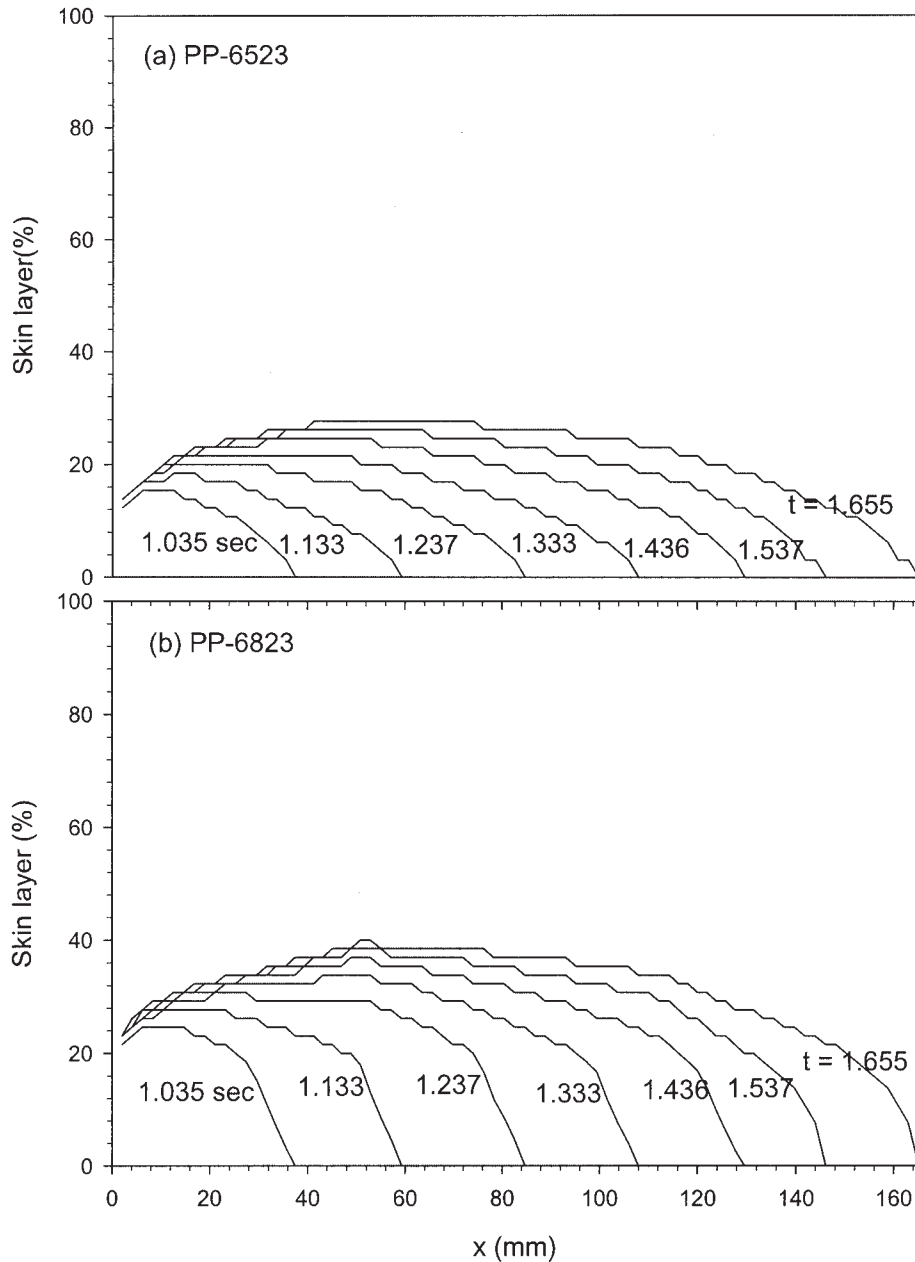
Figure 13 Normalized skin-layer thickness development as a function of x at different filling times (s) for (a) PP-6523 and (b) PP-6823. The molding conditions were $Q = 12.7$ cm^3/s, $T_w = 60°$C, $t_h = 45$ s, and $T_0 = 215°$C.

increase in the skin-layer thickness as the mold-wall temperature is reduced. It is understandable that the lower mold temperature provides greater cooling effects during the injection molding. At a certain gapwise location away from the mold wall, this leads to lower T_m's and, therefore, higher relaxation times of the melt during the molding cycle. As a result of this effect, the extent of the molecular orientation increases, and this gives rise to an increase in the skin-layer thickness.

Figure 14(c) shows the effect of the injection speed on the skin-layer thickness of the moldings. The skin layer is thinner at the higher injection speed. However, because a higher injection speed generally gives

rise to higher shear rates for the melt during the filling stage, the opposite trend should be expected. The occurrence of flow-induced crystallization with the addition of a highly oriented crystalline microstructure largely depends on the extent of molecular deformation due to flow. For a given polymer undergoing a given temperature history, there are two factors affecting the extent of molecular orientation. One is the deformation intensity, that is, the shear rate, and the other is the shearing time. A lower injection speed allows the molten polymer to experience a longer shearing time during the filling stage. On the other hand, a longer shearing time allows the melt to be cooled more effectively during the filling stage. The
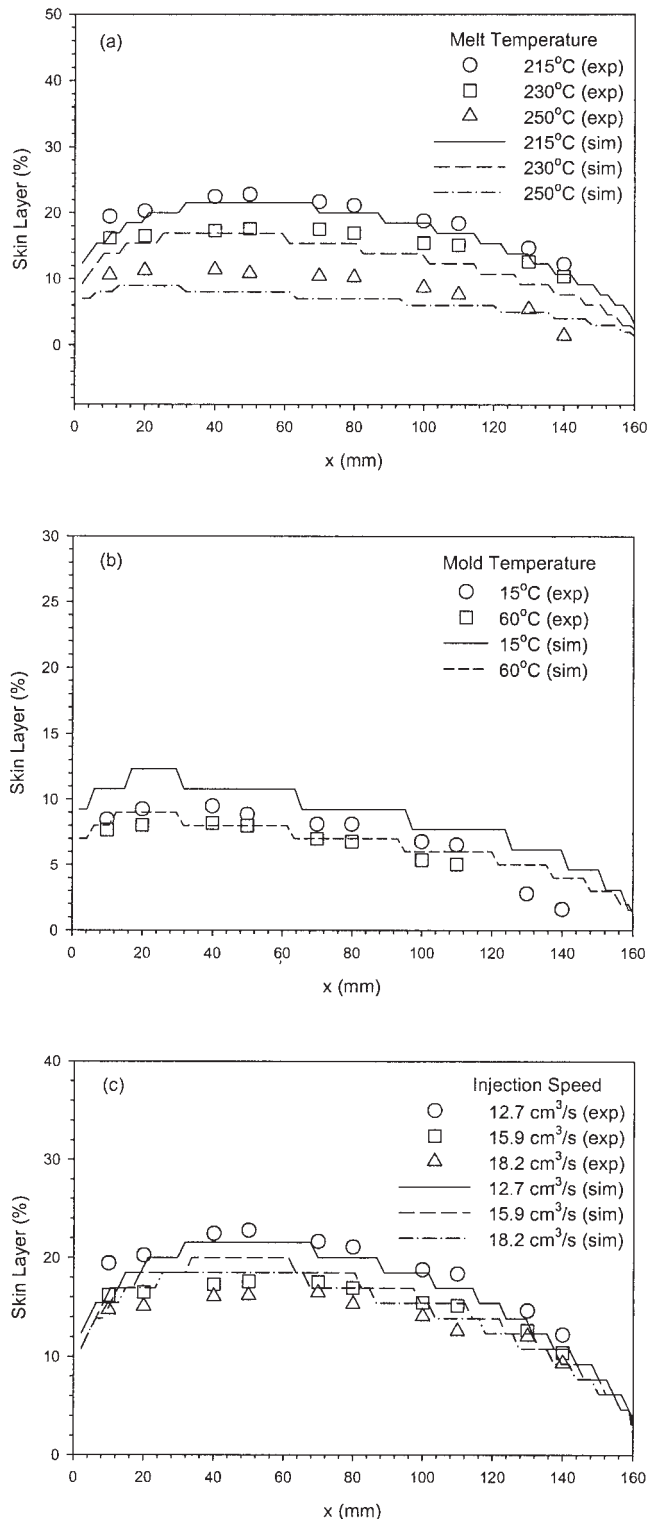
Figure 14 Measured (symbols)[67] and predicted (lines) normalized skin-layer thickness as a function of x for PP-6523 moldings obtained (a) at various inlet T_0's ($Q = 12.7$ cm^3/s, $T_w = 60°$C, and $t_h = 45$ s), (b) at various mold temperatures ($Q = 12.7$ cm^3/s, $T_0 = 250°$C, and $t_h = 45$ s), and (c) at various injection speeds ($T_0 = 215°$C, $t_h = 45$ s, and $T_w = 65°$C)

latter results in a higher shear rate at locations farther away from the mold wall because of an increase in the viscosity. Consequently, the extent of molecular orientation increases at these locations as the injection speed decreases. Therefore, because of the overall increase in the molecular orientation and the polymer being in its supercooled state, the highly oriented crystallite microstructure develops at locations farther away from the wall.

Figure 15 presents the developed skin-layer thickness as a function of x for PP-6523, PP-6723, and PP-6823. Both the simulated and experimental results[67] show that under similar molding conditions, PP-6823 has a tendency of producing a significantly thicker skin layer. This is due to the fact that the elastic property of the high-molecular-weight polymer contributes to higher stress buildup and higher elevation of T_m^0. The latter causes a higher degree of supercooling, which enhances flow-induced crystallization. Therefore, a thicker skin layer appears. At the same time, Figure 6(a) shows that iPP with a higher molecular weight exhibits a lower critical shear rate of flow-induced crystallization. During the filling stage, this also gives rise to greater molecular orientation of iPP with a higher molecular weight. Again, a higher molecular orientation is favorable to the development of a thicker skin layer.

Concerning the effect of the processing parameters on PP-6723 and PP-6823 moldings, the measured and predicted skin-layer thicknesses indicate similar influences, including the injection speed, inlet T_0 value, and mold temperature. Finally, the observations made in this experimental study and in simulations based on the developed crystallization model regarding the effects of the processing parameters on the skin-layer thickness of the moldings are in good agreement with experimental and theoretical studies reported earlier.[42,43,45,48] However, the main advantage of this theoretical description, in comparison with earlier attempts, is that it does not require us to generate a tremendous amount of experimental data to characterize flow-induced crystallization. In this approach, flow-induced crystallization is predicted through the use of a nonlinear viscoelastic constitutive equation, with the parameters of the model measured with basic rheological experiments.

CONCLUSIONS

During the processing of a crystallizing polymer, flow-induced crystallization inherently occurs under nonisothermal flow conditions. Thus, flow-induced crystallization plays a major role in determining the resultant crystallinity and microstructure, influencing the end-use physical and optical properties of moldings. In an attempt to predict flow-induced crystallization in the moldings of crystallizing polymers, we
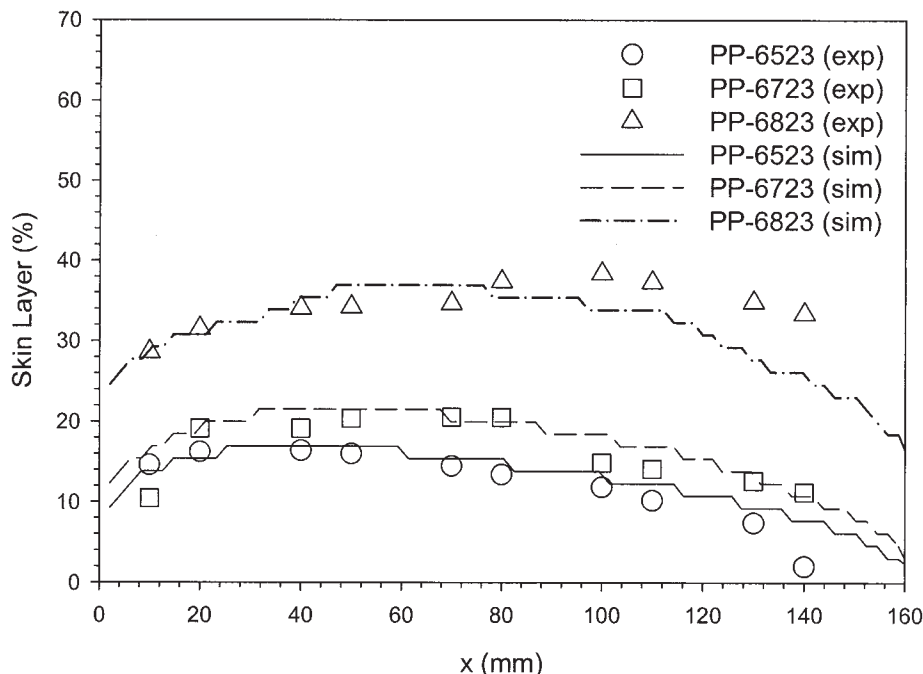
Figure 15 Measured (symbols)[67] and predicted (lines) normalized skin-layer thickness as a function of x for PP-6523, PP-6723, and PP-6823. The molding conditions were $Q = 12.7$ cm^3/s, $T_0 = 230°$C, $t_h = 45$ s, and $T_w = 60°$C.

performed viscoelastic process simulations of injection molding. Flow-induced crystallization was investigated via thermodynamic considerations through the entropy changes between unoriented and oriented melts by means of a nonlinear viscoelastic constitutive equation. T_m due to flow was calculated with the reduction of the entropy. This allowed us to calculate the position in the cavity at which flow-induced crystallization took place.

For the iPPs studied here, the gapwise crystallinity distribution was rather flat and showed little dependence on the processing conditions. However, the thickness of the highly oriented skin layer in the moldings was very sensitive to the processing variables. In particular, the skin-layer thickness decreased with an increase in the injection speed, inlet T_0 value, and mold temperature. The effect of the molecular weight on the formation of the highly oriented skin layer was quite pronounced. The predicted results were well matched by the experimental data for the skin-layer thickness.

References

1. Hoffman, I. D.; Davis, G. T.; Lauritzen, S. I. In Treatise on Solid State Chemistry; Hannay, N. B., Ed.; Plenum: New York, 1976; Vol. 3, Chapter 7.
2. Nakamura, K.; Watanabe, T.; Katayama, K.; Amano, T. J Appl Polym Sci 1972, 16, 1077.
3. Nakamura, K.; Katayama, K.; Amano, T. J Appl Polym Sci 1973, 17, 1031.
4. Schneider, W.; Koeppl, A.; Berger, J. Int Polym Process 1988, 2, 151.
5. Avrami, M. J Chem Phys 1939, 7, 1103.
6. Avrami, M. J Chem Phys 1940, 8, 212.
7. Avrami, M. J Chem Phys 1941, 9, 177.
8. Kolmogoroff, A. N. Izv Akad Nauk Ser Math 1937, 1, 355.
9. Evans, U. R. Trans Faraday Soc 1945, 41, 365.
10. Schultz, J. M.; Petermann, J. Colloid Polym Sci 1984, 262, 294.
11. Petermann, J.; Schultz, J. M. Colloid Polym Sci 1984, 262, 217.
12. Tiller, W. A.; Schultz, J. M. J Polym Sci Polym Phys Ed 1984, 22, 143.
13. Schultz, J. M. Polym Eng Sci 1991, 31, 661.
14. Bushman, A. C.; McHugh, A. J. J Polym Sci Part B: Polym Phys 1997, 35, 1649.
15. Dairanieh, I. S.; McHugh, A. J.; Doufas, A. K. Soc Plast Eng Annu Tech Conf 1998, 56(1), 212.
16. Doufas, A. K.; McHugh, A. J.; Miller, C. J Non-Newtonian Fluid Mech 2000, 92, 27.
17. Doufas, A. K.; McHugh, A. J.; Miller, C.; Immaneni, A. J Non-Newtonian Fluid Mech 2000, 92, 81.
18. McHugh, A. J.; Doufas, A. K. Compos A 2001, 32, 1059.
19. Ziabicki, A. Colloid Polym Sci 1974, 252, 207.
20. Ziabicki, A.; Jarecki, L. In High-Speed Fiber Spinning; Ziabicki, A.; Kawai, H., Eds.; Wiley: New York, 1985; p 225.
21. Ziabicki, A. J Non-Newtonian Fluid Mech 1988, 30, 141.
22. Ziabicki, A.; Tian, J. J Non-Newtonian Fluid Mech 1993, 47, 57.
23. Eder, G.; Janeschitz-Kriegl, H. Colloid Polym Sci 1988, 266, 1087.
24. Eder, G.; Janeschitz-Kriegl, H.; Krobath, G. Prog Colloid Polym Sci 1989, 80, 1.
25. Eder, G.; Janeschitz-Kriegl, H.; Liedauer, S. Prog Polym Sci 1990, 15, 629.
26. Eder, G.; Janeschitz-Kriegl, H.; Liedauer, S. Prog Colloid Polym Sci 1992, 87, 129.
27. Flory, P. J. J Chem Phys 1947, 15, 397.
28. Gaylord, R. J. J Polym Sci Polym Phys Ed 1976, 14, 1827.

29. Shimizu, J.; Okui, N.; Kikutani, T. In High-Speed Fiber Spinning; Ziabicki, A.; Kawai, H., Eds.; Wiley: New York, 1985; p 173.
30. Katayama, K.; Yoon, M. G. In High-Speed Fiber Spinning; Ziabicki, A.; Kawai, H., Eds.; Wiley: New York, 1985; p 207.
31. Chen, S.; Yu, W.; Spruiell, J. E. J Appl Polym Sci 1987, 34, 1477.
32. Yeh, G. S. Y. Polym Eng Sci 1976, 16, 145.
33. Yeh, G. S. Y. Polym Eng Sci 1976, 16, 138.
34. Yeh, G. S. Y.; Hong, K. Z. Polym Eng Sci 1979, 19, 395.
35. Yeh, G. S. Y.; Hong, K. Z.; Krueger, D. L. Polym Eng Sci 1979, 19, 401.
36. Keller, A.; Machin, M. J. J Macromol Sci Phys 1967, 1, 41.
37. Treloar, L. R. G. The Physics of Rubber Elasticity, 2nd ed.; Clarendon: Oxford, 1958; p 342.
38. Mark, J. E. J Chem Educ 1981, 58, 898.
39. Haas, T. W.; Maxwell, B. Polym Eng Sci 1969, 9, 225.
40. Ishizuka, O.; Koyama, K. Polymer 1977, 18, 913.
41. Isayev, A. I.; Chan, T. W.; Shimojo, K.; Gmerek, M. J Appl Polym Sci 1995, 55, 807.
42. Isayev, A. I.; Chan, T. W.; Gmerek, M.; Shimojo, K. J Appl Polym Sci 1995, 55, 821.
43. Demiray, M.; Isayev, A. I. Soc Plast Eng Annu Tech Conf 1996, 54(2), 1576.
44. Chan, T. W.; Isayev, A. I. Polym Eng Sci 1994, 34, 461.
45. Isayev, A. I.; Guo, X.; Guo, L.; Demiray, M. Soc Plast Eng Annu Tech Conf 1997, 55(2), 1517.
46. Isayev, A. I.; Catignani, B. F. Polym Eng Sci 1997, 37, 1526.
47. Guo, X.; Isayev, A. I.; Guo, L. Polym Eng Sci 1999, 39, 2096.
48. Guo, X.; Isayev, A. I.; Demiray, M. Polym Eng Sci 1999, 39, 2132.
49. Guo, X.; Isayev, A. I. Int Polym Process 1999, 14, 377.
50. Guo, X.; Isayev, A. I. Int Polym Process 1999, 14, 387.
51. Palluch, K. P.; Isayev, A. I. Proceedings of the 13th International Congress on Rheology, Cambridge, England, 2000; Vol. 2, p 94.
52. Kim, K. H.; Isayev, A. I.; Kwon, K. Soc Plast Eng Annu Tech Conf 2003, 61(1), 713.
53. Leonov, A. I. Rheol Acta 1976, 15, 85.
54. Sobhanie, M.; Isayev, A. I. Rubber Chem Technol 1989, 62, 939.
55. Ziabicki, A.; Jarecki, L.; Wasiak, A. Comput Theor Polym Sci 1998, 8, 143.
56. Injection and Compression Molding Fundamentals; Isayev, A. I., Ed.; Marcel Dekker: New York, 1987.
57. Hoffman, J. D. Soc Plast Eng Trans 1964, 4, 315.
58. George, H. H. In High-Speed Fiber Spinning; Ziabicki, A.; Kawai, H., Eds.; Wiley: New York, 1985; p 271.
59. Kobayashi, K.; Nagasawa, T. J Macromol Sci Phys 1970, 4, 331.
60. Hay, I. L.; Jaffe, M.; Wissbrun, K. F. J Macromol Sci Phys 1976, 12, 423.
61. Alfonso, G. C.; Grimaldi, D.; Turturro, A. Conv Ital Sci Macromol 1977, 3, 144.
62. Oono, R.; Miasaka, K.; Ishikawa, K. J Polym Sci Polym Phys Ed 1973, 11, 1477.
63. Kraus, G.; Gruver, J. T. J Polym Sci Polym Phys Ed 1972, 10, 2009.
64. Dunning, W. J. Trans Faraday Soc 1954, 50, 1115.
65. Guo, J.; Narh, K. A. Adv Polym Technol 2002, 21, 214.
66. Chan, T. V.; Shyu, G. D.; Isayev, A. I. Polym Eng Sci 1995, 35, 733.
67. Guo, X. Ph.D. Thesis, University of Akron, 1999.
68. Evens, G. A. Practical Numerical Analysis; Wiley: New York, 1995.
69. Catignani, B. M.S. Thesis, University of Akron, 1996.
70. Van Krevelen, D. W. Properties of Polymers; Elsevier: Amsterdam, 1990.